

Luminosity-Metallicity Relation for dIrr Galaxies in the Near-Infrared

Ivo Saviane¹ Valentin D. Ivanov¹ Enrico V. Held² Danielle Alloin³ R. Michael Rich⁴ Fabio Bresolin⁵ and Luca Rizzi⁶ *

¹ European Southern Observatory, Alonso de Cordova 3107, Santiago, Chile
e-mail: isaviane,vivanov@eso.org

² OAPD, vicolo Osservatorio 5, I-35122 Padova, Italy
e-mail: held@pd.astro.it

³ AIM, CEA/DSM/IRFU-Université Paris 7, Service d'Astrophysique, CEA/Saclay, 91191, Gif-sur-Yvette Cedex, France
e-mail: danielle.alloin@cea.fr

⁴ Department of Physics and Astronomy, 430 Portola Plaza, UCLA, Los Angeles, CA 90095-1547, USA
e-mail: rmr@astro.ucla.edu

⁵ Institute for Astronomy, University of Hawaii at Manoa, 2680 Woodlawn Drive, Honolulu, HI 96822, USA
e-mail: bresolin@ifa.hawaii.edu

⁶ Joint Astronomy Centre, 660 N. O'hoku Place, University Park, Hilo, HI 96720, USA
e-mail: l.rizzi@jach.hawaii.edu

Received 05/04/2007; Accepted 22/05/2008

Abstract

Context. The luminosity-metallicity relation is one of the fundamental constraints in the study of galaxy evolution; yet none of the relations available today has been universally accepted by the community.

Aims. The present work is a first step to collect homogeneous abundances and near-infrared (NIR) luminosities for a sample of dwarf irregular (dIrr) galaxies, located in nearby groups. The use of NIR luminosities is intended to provide a better proxy to mass than the blue luminosities commonly used in the literature; in addition, selecting group members reduces the impact of uncertain distances. Accurate abundances are derived to assess the galaxy metallicity.

Methods. Optical spectra are collected for H II regions in the dIrrs, allowing the determination of oxygen abundances by means of the temperature-sensitive method. For each dIrr galaxy H-band imaging is performed and the total magnitudes are measured via surface photometry.

Results. This high-quality database allows us to build a well-defined luminosity-metallicity relation in the range $-13 \geq M_H \geq -20$. The scatter around its linear fit is reduced to 0.11 dex, the lowest of all relations currently available. There might exist a difference between the relation for dIrrs and the relation for giant galaxies, although a firm conclusion should await direct abundance determinations for a significant sample of massive galaxies.

Conclusions. This new dataset provides an improved luminosity-metallicity relation, based on a standard NIR band, for dwarf star-forming galaxies. The relation can now be compared with some confidence to the predictions of models of galaxy evolution. Exciting follow-ups of this work are (a) exploring groups with higher densities, (b) exploring nearby galaxy clusters to probe environmental effects on the luminosity-metallicity relation, and (c) deriving direct oxygen abundances in the central regions of star-forming giant galaxies, to settle the question of a possible dichotomy between the chemical evolution of dwarfs and that of massive galaxies.

Key words. Galaxies: fundamental parameters; Infrared: galaxies; Galaxies: dwarf; Galaxies: irregular; Galaxies: ISM

1. Introduction

According to standard scenarios of galactic chemical evolution, a luminosity-metallicity (L-Z) relation is established through galactic winds – induced by supernova explosions – removing the interstellar medium (ISM) before it has been totally converted into stars (see the seminal work of Larson 1974; and also Tinsley & Larson 1979, Dekel & Silk 1986, Lynden-Bell 1992, among others). As this process is more efficient in low-mass (low escape velocity) galaxies, less metals should be trapped

in dwarf galaxies. Indeed, a well-defined L-Z relation is observed in spheroidal galaxies (e.g. Caldwell et al. 1992), mostly field galaxies, in which old stellar populations dominate, and for which the chemical evolution has stopped. Do we expect a similar behaviour in the case of dwarf irregular galaxies (dIrr)? The situation is more complex. First, dIrrs are still active (in the sense of star formation), exhibiting substantial gas fractions and a broad range of star-formation rates (SFR). So, one would expect to encounter in Irrs, ISMs of different chemical maturities and rapidly evolving luminosities: all factors which would loosen any established relation between mass and metallicity. Second, the available sample of dIrrs is made of galaxies belonging to groups rather than distributed in the field. It is well known that the evolution of a galaxy gas content depends on its environment, and that gas stripping is boosted through galaxy interactions in dense groups and cluster sub-clumps. So, while one can see reasons why the terminal chemical evolution in dIrrs

Send offprint requests to: isaviane@eso.org

* Based on data collected at the European Southern Observatory, La Silla, Chile, Proposal N. 70.B-0424(A,B); Based on observations made at Lick (UCO) Observatory; Based on observations made with the William Herschel Telescope operated on the island of La Palma by the Isaac Newton Group in the Spanish Observatorio del Roque de los Muchachos of the Instituto de Astrofísica de Canarias.

might depend on the galactic mass – similarly to the sample of gas-free spheroidal galaxies –, there are a number of extra processes blurring the situation. Hence, it is unclear whether dIrr galaxies should exhibit a luminosity-metallicity relation.

Under such a scenario dwarf galaxies lose substantial fractions of their mass in the course of their evolution, and should be major contributors to the chemical evolution of the inter-galactic medium (IGM). In particular, mass loss through galactic winds should occur in dIrr galaxies: their study contributes to probe the fraction of the IGM enrichment which is due to dwarf galaxies in general (e.g., Garnett 2002). Losses of enriched gas in dwarf galaxies have indeed been observed: Martin et al. (2002) detected a galactic wind of $\sim 6 \times 10^6 M_\odot$ from NGC 1569, and for the first time, they could measure its metallicity. The authors concluded at $3 \times 10^4 M_\odot$ of oxygen in the wind, almost as much as in the disk of the dwarf itself. Hence, the cosmic chemical evolution and the existence of an L-Z relation appear to be closely inter-related: this was an additional motivation to pursue the study presented here.

The case of another dIrr, SagDIG, further illustrates this point. In one of our previous studies (Saviane et al. 2002) we measured a very low oxygen content ($7.26 \leq 12 + \log(\text{O}/\text{H}) \leq 7.50$), a result which is not compatible with a closed-box evolution. According to the model, such a low abundance would imply a large gas mass fraction $\mu = m_{\text{gas}}/(m_{\text{gas}} + m_{\text{stars}}) \approx 0.97$, whereas the observed gas mass fraction is only $\mu \approx 0.86$. It is easy to compute that $\approx 1.5 \times 10^6 M_\odot$ of gas are missing, and, since this mass is smaller than that of the NGC 1569 galactic wind, it is plausible to conclude that SagDIG lost some of its gas into the IGM.

On the other hand, a cautionary remark should be added, since a general consensus on the role of galactic winds in the evolution of dwarf galaxies and the IGM has not been reached yet. For example by means of chemo-photometric models Calura & Matteucci (2006) conclude that dIrr galaxies play a negligible role in the enrichment of the IGM, and the numerical models of Silich and Tenorio-Tagle (1998) show that that galactic winds never reach the escape velocity of these dwarfs. And in the case of dwarf spheroidal (dSph) galaxies, the 3D hydrodynamic simulations of Marcolini et al. (2006) show that no galactic winds develop in these objects.

In our attempt to place SagDIG on previously established L-Z relations for dIrr galaxies, we realized that the existence of such a relation was controversial. Some studies had concluded at very well-defined correlations (Skillman et al. 1989; Richer & McCall 1995; Pilyugin 2001), others have found only mild relations with substantial scatter (e.g. Skillman et al. 2003b), or no correlation at all (Hidalgo Gámez & Olofsson 1998; Hunter & Hoffman 1999). Perhaps the major source of confusion in these investigations comes from the ill-defined samples used in the analysis. Abundance data are taken from different sources (with spectra of variable quality and processed through different reduction and analysis techniques); apparent luminosities and distances are taken from catalogs, meaning that they are largely approximate. Moreover, although the L-Z relation is expected to depend on the environment, this is rarely taken into account in the analysis. Another main source of uncertainty is the common use of the blue absolute magnitude as a tracer of the mass. Optical luminosities can in fact be extremely misleading in Irr galaxies, because of their star-bursting activity (e.g. Tosi et al. 1992 or Schmidt et al. 1995). Already, Bruzual & Charlot (1983) showed that at 400 nm a 1 Myr old burst is \sim three orders of magnitude brighter than an underlying old (15 Gyr) stellar population of comparable mass. In other words, a dwarf galaxy host-

ing a recent starburst could be as luminous, in the blue, as a galaxy orders of magnitudes more massive but lacking a recent star formation episode. In comparison, a recent starburst is at most 10 times brighter in the near-infrared (NIR) than its underlying old population of same mass. Therefore, the NIR window being more stable with regard to star formation episodes is more appropriate for probing the galaxy basic properties, such as its mass.

In order to address these issues, we embarked on a medium-term project aimed at gathering nebular oxygen abundances and NIR luminosities for a sample of dIrrs belonging to the three nearest groups of galaxies. In this way we can test the existence of an L-Z relation in well-defined environments (characterized by the group density), for which the scatter in apparent distance modulus is low, and for which an homogeneous set of abundances can be obtained.

Since we started the project, a few investigations have been published, in relation with the context presented above. The first L-Z relation using NIR luminosities (aside the work by Saviane et al. 2004) is that by Salzer et al. (2005; hereafter S05). Their sample is dominated by massive galaxies, and their relation was derived using 2MASS data for the luminosities, and proprietary spectra from the KPNO International Spectroscopic Survey (KISS) for the metallicities. The 2MASS survey having a relatively shallow limiting magnitude, for a few additional dwarf galaxies NIR photometry was supplemented by the authors. At the other extreme, the sample assembled by Mendes de Oliveira et al. (2006) is entirely made of dwarf galaxies. They gathered *K*-band luminosities and metallicities – obtained through the direct method – for 29 dIrrs. The NIR data are from 2MASS or from Vadvuescu et al. (2005), and metallicities have been picked up from a variety of sources. Finally Lee et al. (2006) have used the *Spitzer* Infrared Array Camera to compute $4.5 \mu\text{m}$ luminosities for ~ 30 nearby dIrrs, the distance of which have been derived using standard candles. With oxygen abundances collected from the literature, they constructed a $4.5 \mu\text{m}$ L-Z relation.

Although these studies have certainly improved the situation, they do not represent the ideal case yet. S05 abundances are derived through a new but indirect method, and the sample is very scarce in dwarf galaxies. Yet, S05 is the only study which includes *H*-band photometry, so a comparison with their L-Z relation is carried out later in this paper, in Sect. 5.3. As extensively discussed in Sect. 5.2, the use of heterogeneous data from the literature may produce a different L-Z relation than the one obtained with an homogeneous dataset, a likely consequence of distance uncertainties. Therefore, we anticipate that the relation by Mendes de Oliveira et al. (2006) will need to be revised once a better controlled sample, with *K*-band photometry, becomes available. Finally, the use of a non-standard passband does not allow an easy comparison of the L-Z relation by Lee et al. (2006) to other L-Z relations. For example they need to make several successive assumptions in order to convert their luminosities into masses, and then compare the mass-metallicity relation to the SDSS one. For all these reasons, we believe that so far our approach stands as the one with the smallest number of uncertainties and the broadest applicability.

The paper is structured as described below. In Sect. 2 we explain how the targets were selected, and give a brief account of the data reduction techniques – described in more detail in the appendices –. The computation of chemical abundances is described in Sect. 3, where we also compare our results with previous abundance determinations. The resulting NIR luminosity-metallicity relation for dIrr galaxies is presented in Sect. 4. It is discussed in Sect. 5, with a possible explanation of its origin pre-

Table 1. Target list

Main ID	Other IDs	
	M81 group	
DDO 42	NGC 2366	UGC 03851
KDG 52	M81 dw A	PGC 023521
DDO 53	UGC 4459	VII Zw 238
UGC 4483		
KDG 54	UGC 4945	UGCA 158
candidate 5	[FM2000] 5	
BK 3N	PGC 028529	
DDO 66	UGC 05336	Holmberg IX
DDO 82	UGC 5692	
DDO 165	UGC 8201	VII Zw 499
	Sculptor group	
ESO 347-G017		
UGCA 442	ESO 471- G 006	AM 2341-321
ESO 348-G009	AM 2346-380	UKS 2346-380
NGC 59	ESO 539- G 004	
ESO 294-G010	AM 0024-420	
ESO 473-G024	AM 0028-23	
AM0106-382	LEDA 166061	[KK98] 011
NGC 625	ESO 297- G 005	AM 0132-414
ESO 245-G005	AM 0142-435	A143

sented in Sect. 5.1 and its comparison with a relation based on literature data in Sect. 5.2. In Sect. 5.3 we discuss the possible dwarf vs. giant galaxy dichotomy, through a comparison of our results to those by Salzer et al. (2005). Finally a summary and the conclusions of this study are provided in Sect. 6.

2. The data set

2.1. Target selection

The next two sections describe how the targets were selected in each of the two groups. The most popular galaxy names are listed in Table 1, together with other aliases.

2.1.1. Sculptor group

Sculptor group Irr galaxies were selected from the list of Côté et al. (1997; hereafter C97). The seven galaxies with H α detection and radial velocities $v_r < 1000 \text{ km s}^{-1}$, were included in our target list shown in Table 2. Note that the C97 catalog contains another set of galaxies with velocities between 1000 and 2000 km s^{-1} , as well as sources with velocities up to $\sim 17000 \text{ km s}^{-1}$. In addition to our main list, we included ESO 294-G010, which has been classified as intermediate dS0/Im by Jerjen et al. (1998; hereafter J98) and, although C97 measured an H α velocity $v_r = 4450 \text{ km s}^{-1}$, a much smaller velocity is quoted in NED. Moreover, J98 have detected [O III] and H α emission, albeit very weak. Yet, as no emission was detected during our H α pre-imaging, we did not carry over further observations: it is possible that J98 detected a PN with H α emission below our detection threshold. Bouchard et al. (2005) re-classified this galaxy as dSph/dIrr.

The main observational campaign was carried out in October 2002: NIR imaging of the seven targets was collected, while bad weather undermined the spectroscopic observing run and spectra could be collected for five targets only. A few months after the completion of our observations, Skillman et al. (2003a;

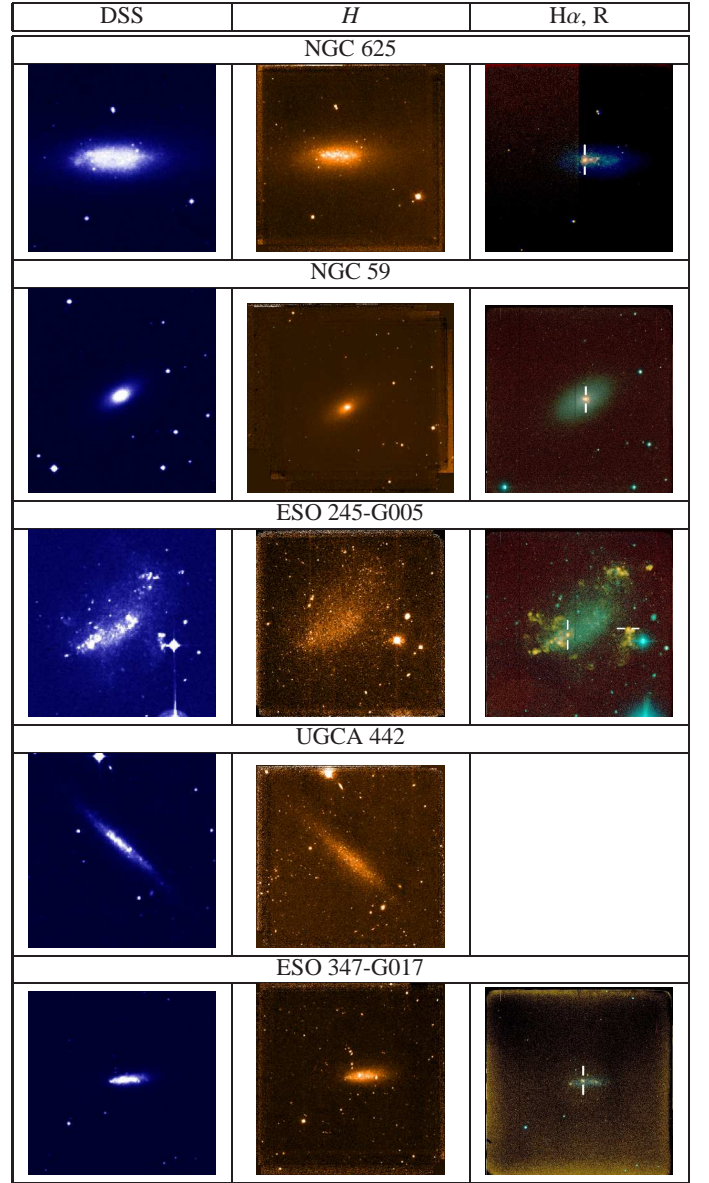


Figure 1. From left to right, we show the morphology of the Sculptor group targets in the optical (DSS), infrared H (SOFI), and a false-color montage of H α and R (EFOSC2) images. The reddish, diffuse nebulae in the right image are H II regions, and the vertical ticks mark those for which spectra have been obtained. The galaxy luminosity decreases from top to bottom panels, with the exception of ESO 294 G010, which was not observed in the NIR. In all images, North is up and East to the left, and the field of view is $\sim 5' \times 5'$.

hereafter S03a) identified other dwarfs showing H α emission despite a null detection by C97, bringing the total number of actively star-forming dIrrs in the Sculptor group up to twelve. In a companion paper, Skillman et al. (2003b; hereafter S03b) derived oxygen abundances for five of these galaxies (reported in Table 7), two of them being in common with our original sample. So, to improve the comparison with S03b, in August 2003 we complemented our data set with NIR imaging and long-slit spectroscopy for ESO 473-G024. Finally, ESO 245-G005 was re-observed in October 2003, in order to measure an H II region closer to the center of the galaxy.

Table 2. Observations of Sculptor group targets. Additional data are the radial velocity from Côté et al. (1997), and the radial velocity from the NASA extragalactic database. No emission was detected in the H α pre-imaging for ESO 294-G010.

Galaxy	Target list		Journal of the observations						
	R.A.	Dec.	v_r [km/sec]		EFOSC2		SOFI		airm.
	J2000		C97	NED	Date	t [s]	Date	t [s]	
ESO 347-G017	23:26:56.0	-37:20:49	659	692 \pm 4	13 Oct 2002	3 \times 1800	15 Oct 2002	3420	1.10
					14 Oct 2002	2 \times 1800	16 Oct 2002	300	1.02
UGCA 442	23:43:45.5	-31:57:24	283	267 \pm 2			16 Oct 2002	3600	1.08
ESO 348-G009	23:49:23.5	-37:46:19	628	648 \pm 4			16 Oct 2002	3600	1.09
NGC 59	00:15:25.1	-21:26:40	357	382 \pm 60	13 Oct 2002	4 \times 1800	15 Oct 2002	4080	1.05
							16 Oct 2002	300	1.02
ESO 294-G010	00:26:33.4	-41:51:19	4450	117 \pm 5			
ESO 473-G024	00:31:23.1	-22:46:02	...	541 \pm 1	19 Aug 2003	3 \times 1200	10 Aug 2003	1560	1.10
AM 0106-382	01:08:21.9	-38:12:34	645	645 \pm 10	14 Oct 2002	4 \times 1800	15 Oct 2002	3480	1.26
							16 Oct 2002	1800	1.15
NGC 625	01:35:04.2	-41:26:15	415	396 \pm 1	14 Oct 2002	3 \times 900	15 Oct 2002	1020	1.71
							16 Oct 2002	900	1.78
ESO 245-G005	01:45:03.7	-43:35:53	389	391 \pm 2	13 Oct 2002	2 \times 1800	16 Oct 2002	2460	1.32
					14 Oct 2002	3 \times 1800			
					14 Oct 2003	3 \times 1200			

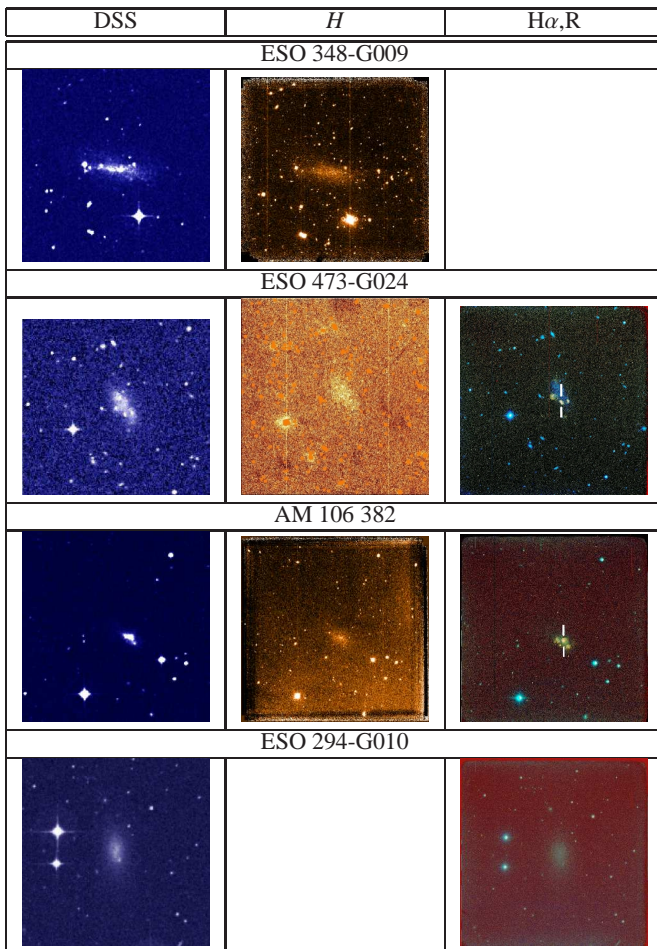


Figure 1. (continued)

In summary, with the observations presented here there are now eight Sculptor group dwarfs with measured abundances, of which three are in common between our study and S03b. NIR data are available for all eight objects.

2.1.2. M81 group

A first list of M81 group members has been compiled by Karachentseva et al. (1985; hereafter K85), by inspecting photographic plates taken at the 6-m telescope. It includes 14 probable and 11 questionable members (on the basis of radial velocity and visual appearance), all of them of dIrr type. Later, Karachentseva & Karachentsev (1998) added six new possible members in the dE class, by searching POSS-II and ESO/SERC films. A search based on CCD imaging was carried out by Caldwell et al. (1998), who, however, did not publish their catalog. Finally, Froebrich & Meusinger (2000; hereafter FM00) discovered six more candidates in a survey that employed digitally stacked Schmidt plates. The candidates are equally divided into dE and dIrr types. A new version of the catalog of M81 member candidates was recently published by Karachentsev et al. (2002; hereafter K02), showing a few additions and a few deletions when compared to the previous catalog.

Ten M81 group dwarfs have been observed from 2001 to 2002 (Table 3). Our first run was with the *Kast* spectrograph at Lick: the instrument offers limited imaging capabilities, so we selected the target H II regions with the following strategy. The slit was first placed on the brightest nebosity within a target dwarf and a short-exposure spectrum was taken. If it showed a conspicuous H α line, then the integration was continued, otherwise we moved to another candidate region and tried again. If no emission was detected in two to three regions (depending on the galaxy luminosity), we moved to the next dwarf target. With this procedure, emission was detected in only half of the galaxies, namely DDO 42, DDO 53, UGC 4483, DDO 82, and KDG 54 (which turned out to be a background, higher redshift object). No emission was detected in KDG 52, BK 3N, DDO 66, DDO 165, nor in the candidate 5 of Froebrich & Meusinger (2000). For objects which did show emission lines, the spectroscopic observations were followed-up by NIR imaging performed with the INGRID camera at the ING/WHT telescope on La Palma.

After the completion of the spectroscopic observations, three H α surveys including M81 group galaxies were published by Hunter & Elmegreen (2004), Gil de Paz et al. (2003), and James et al. (2004). These surveys have detected emission-line regions in, among others, DDO 42, DDO 53, UGC 4483, DDO 66, DDO 82, and DDO 165. So they confirm our detections, but they

Table 3. Observations of M81 group targets. The group membership has been established in K85, except for the candidate 5 which comes from Froebrich & Meusinger (2000). Additional data are the radial velocity from the NASA extragalactic database. Exposure times for the *Kast* spectrograph observations are flagged with a code indicating the instrument setup: B=blue arm with grism 830/3460; R=red arm with grating 300/4230; BR=both arms with dichroic D46; F=red arm without dichroic; HR=red arm with grating 1200/5000 centered around H α . A ‘n.e.’ in the INGRID observation means that no emission was detected and so, no NIR imaging had been performed.

Target list				Journal of the observations					
Galaxy Main ID	R.A. J2000	Dec.	v_r [km/sec]	<i>Kast</i>		INGRID			
					t [s]	Date	t [s]	airm.	
DDO 42	07:28:53.7	+69:12:54	+80	17 Dec 2001	600+2×1200 RB	15 Jan 2003	3600	1.36	
				17 Dec 2001	1800 B + 1800 HR	16 Jan 2003	300	1.46	
				17 Dec 2001	600 F + 600 HR				
				14 Jan 2002	600+2×1200 RB				
				14 Jan 2002	1800 B + 1800 HR				
KDG 52	08:23:56.0	+71:01:45	+113	15 Jan 2002	1800 B + 1800 HR				
				17 Dec 2001	2 ×300 RB		n.e.		
				DDO 53	08:34:07.2	+66:10:54	+20	17 Dec 2001	3 ×1800 RB
UGC 4483	08:37:03.0	+69:46:50	+156	17 Dec 2001	1800 HR + 1800 B				
				14 Jan 2002	2 ×1200 RB	15 Jan 2003	960	1.29	
KDG 54	09:22:25.2	+75:45:57	+659	14 Jan 2002	1800 B + 1800 HR	16 Jan 2003	3210	1.34	
				candidate 5	09:39:02.0	+69:25:01	...	14 Jan 2002	2 ×(1200+1800) RB
BK 3N	09:53:48.5	+68:58:08	−40				n.e.		
DDO 66	09:57:30.1	+69:02:52	+46				n.e.		
DDO 82	10:30:34.8	+70:37:14	+56	15 Jan 2002	300 + 2×600 RB	16 Jan 2003	3600	1.41	
DDO 165	13:06:24.8	+67:42:25	+31	15 Jan 2002	3×1200 RB				
							n.e.		

also unveil emission-line regions in DDO 66 and DDO 165, for which our trial-and-error technique gave a null result.

2.2. Optical spectrophotometry

2.2.1. Sculptor group

The observations summarized in Table 2 were carried out using EFOSC2 (ESO Faint Object Spectrograph and Camera, 2; Buzzoni et al. 1984) at La Silla. Most spectra were taken on October 13 and 14, 2002, an additional spectrum of ESO245-G005 was collected on October 14, 2003, and finally ESO473-G024 was observed in August 2003. EFOSC2 is a multi-mode instrument working at the Cassegrain focus of the ESO/3.6m telescope, allowing both imaging and long-slit, low-resolution spectroscopy. A camera images the aperture onto a 2048 × 2048 px Loral/Lesser, thinned, and UV-flooded CCD. Its pixel size is 15 μ m, which corresponds to 0''.157 on the sky, for a total field of view of $5.4 \times 5.4'$. Under normal operation, the CCD is read out by the left amplifier at a gain of $1.3e^-/ADU$, and since numerical saturation occurs at $2^{16}ADU$, it remains well below the full well capacity of 104,000 e^-px^{-1} . The dark current is $7e^-px^{-1}hr^{-1}$, comparable to the readout noise of $\sim 10e^-px^{-1}$. The CCD was binned at 2×2 both in imaging and spectroscopy mode. Indeed, rebinning allows the line profile of the calibration arcs to be sampled with more than four pixels, even with the highest dispersion grisms and a 0''.5 wide slit, so for spectroscopic observations there is no real advantage in using the 1×1 binning mode.

For each galaxy, the target H II regions were identified by subtracting a 5 min R image from a 15 min H α image, and the slit was then centered on the brightest region. Maps of the H II regions are shown in Fig. 1. During the night, two spectrophotometric standards (Feige 110 and LTT 3218) from Oke (1990) and Hamuy et al. (1992, 1994) were observed. Other calibration

frames were taken in the afternoon preceding each observing night (bias, darks, HeAr arcs, and dome flatfields). Grism #11 was used without an order sorting filter, yielding a dispersion of 4.2 \AA px^{-1} and giving a range from 3400 \AA to 7500 \AA . The second order spectrum (appearing at wavelengths longer than $\sim 6800 \text{ \AA}$) is only a few percent of the first order, so the contamination is negligible for the target spectra. It is however important for the determination of the response function. Indeed, it can be seen in the spectrum of the extremely blue standard Feige 110 (spectral type D0), but it disappears already in the spectrum of LTT 3218, although its spectral type is DA. The latter standard was then used to compute the response function. Spectra of the target regions were obtained with a 1'' width slit, while the 5'' width slit, aligned along the parallactic angle, was used for observing the spectrophotometric standards, in order to minimize slit losses. The resolution with the 1'' width slit is $\approx 13 \text{ \AA FWHM}$ (from the HeAr lines near 5000 \AA). All slits cover the entire EFOSC2 field of view.

The reduction and analysis of the spectroscopic data was performed in a standard way, with the main steps: (a) 2D wavelength and distortion calibration; (b) extraction of spectra using the wings of H α to define a good window; (c) flux calibration; (d) measurement of line fluxes in the MIDAS/ALICE¹ framework; (e) correction of fluxes for underlying absorption; (f) correction for internal reddening of the region using the H α /H β ratio; (g) computation of T_e using [O III] lines $\lambda 4363$ and $\lambda 4959, 5007$; and finally (h) computation of nebular abundances using IRAF/IONIC².

¹ ESO-MIDAS is the acronym for the European Southern Observatory Munich Image Data Analysis System which is developed and maintained by the European Southern Observatory

² IRAF is distributed by the National Optical Astronomy Observatories, which are operated by the Association of Universities for Research in Astronomy, Inc., under cooperative agreement with the National Science Foundation.

Table 4. Reddening-corrected fluxes for all H II regions in the Sculptor group dwarfs.

Ion λ [Å]	AM106-382	ESO 245-G005 external	ESO 245-G005 central	ESO 347-G017	ESO 473-G024	NGC 59 #1	NGC 59 #2	NGC 625 #1	NGC 625 #2
[O II] 3726.0	2.007 ± 0.041	1.508 ± 0.018	2.767 ± 0.087	2.191 ± 0.016	0.942 ± 0.023	1.080 ± 0.029	2.716 ± 0.092	1.454 ± 0.019	1.516 ± 0.009
H I 3770.6	0.049 ± 0.016	0.052 ± 0.008
H I 3797.9	0.622 ± 0.086	0.064 ± 0.016	0.063 ± 0.008
He I 3819.6	0.143 ± 0.037	0.424 ± 0.084
H 9 3835.4	0.085 ± 0.016	0.077 ± 0.008
[Ne III] 3868.8	0.513 ± 0.037	0.146 ± 0.016	0.312 ± 0.071	0.348 ± 0.015	0.190 ± 0.021	0.374 ± 0.026	0.932 ± 0.082	0.274 ± 0.015	0.207 ± 0.008
[Ne III]+H 8 3879.0
H 8 3889.1	...	0.151 ± 0.016	0.160 ± 0.070	0.117 ± 0.014	0.155 ± 0.020	0.217 ± 0.026	...	0.247 ± 0.015	0.186 ± 0.008
He I 3970.1	...	0.138 ± 0.014	0.209 ± 0.066	0.163 ± 0.013	0.209 ± 0.018	0.250 ± 0.023	...	0.258 ± 0.015	0.208 ± 0.007
He I 4026.2	0.024 ± 0.013	...
[S II]blend 4072.0
H δ 4101.7	...	0.212 ± 0.013	0.183 ± 0.057	0.172 ± 0.011	0.235 ± 0.016	0.250 ± 0.020	...	0.265 ± 0.013	0.248 ± 0.006
H γ 4340.5	0.518 ± 0.032	0.442 ± 0.010	0.483 ± 0.042	0.438 ± 0.010	0.401 ± 0.012	0.466 ± 0.020	0.481 ± 0.047	0.465 ± 0.010	0.463 ± 0.005
[O III] 4363.2	...	0.032 ± 0.010	0.055 ± 0.037	0.049 ± 0.009	0.045 ± 0.011	0.038 ± 0.020	0.063 ± 0.045	0.028 ± 0.010	0.017 ± 0.004
He I 4471.5	0.027 ± 0.008	0.033 ± 0.013	...	0.035 ± 0.008	0.046 ± 0.004
H β 4861.3	1.000 ± 0.024	1.000 ± 0.008	1.000 ± 0.034	1.000 ± 0.009	1.000 ± 0.007	1.000 ± 0.014	1.000 ± 0.042	1.000 ± 0.009	1.000 ± 0.005
[O III] 4958.9	0.616 ± 0.020	0.588 ± 0.007	1.072 ± 0.036	1.267 ± 0.009	0.786 ± 0.006	1.629 ± 0.016	1.337 ± 0.052	1.421 ± 0.010	1.089 ± 0.005
[O III] 5006.8	1.782 ± 0.024	1.797 ± 0.010	3.223 ± 0.058	3.849 ± 0.013	2.473 ± 0.011	4.883 ± 0.023	2.930 ± 0.057	4.268 ± 0.017	3.304 ± 0.008
[Fe III] 5412.0	...	0.034 ± 0.008
He I 5875.7	0.159 ± 0.030	0.082 ± 0.012	0.104 ± 0.045	0.095 ± 0.011	0.062 ± 0.012	0.106 ± 0.019	0.152 ± 0.056	0.106 ± 0.011	0.093 ± 0.006
[S III] 6312.1	...	0.047 ± 0.014	0.039 ± 0.023	...	0.049 ± 0.012	...
[O I] 6363.8	0.006 ± 0.013	...
H α 6562.8	2.850 ± 0.043	2.594 ± 0.024	2.849 ± 0.103	2.592 ± 0.020	2.849 ± 0.037	2.850 ± 0.032	2.850 ± 0.090	2.850 ± 0.020	2.850 ± 0.011
[N II] 6583.4	0.069 ± 0.103	0.064 ± 0.020	0.029 ± 0.037	0.075 ± 0.032
He I 6678.1	0.016 ± 0.016	0.033 ± 0.017	0.023 ± 0.025	0.031 ± 0.064	0.029 ± 0.015	0.030 ± 0.009
[S II] 6716.5	0.125 ± 0.040	0.134 ± 0.018	0.265 ± 0.068	0.208 ± 0.016	0.089 ± 0.019	0.129 ± 0.025	0.282 ± 0.064	0.130 ± 0.015	0.139 ± 0.009
[S II] 6730.8	0.045 ± 0.040	0.114 ± 0.018	0.164 ± 0.068	0.144 ± 0.017	0.058 ± 0.019	0.105 ± 0.025	0.318 ± 0.065	0.123 ± 0.015	0.097 ± 0.009
He I 7065.3	0.021 ± 0.018	...	0.027 ± 0.028	...	0.027 ± 0.017	0.026 ± 0.011
[Ar III] 7135.8	0.070 ± 0.019	...	0.105 ± 0.029	0.137 ± 0.075	0.110 ± 0.018	0.098 ± 0.011
[O II]blend 7325.0
C H α /H β^a	0.002 ± 0.042	0.000 ± 0.019	0.192 ± 0.076	0.192 ± 0.076	0.191 ± 0.022	0.017 ± 0.028	0.302 ± 0.079	0.042 ± 0.018	0.004 ± 0.010

Notes: (a) The reddening constant is computed by the expression: $I_{H\alpha}/I_{H\beta} = I_{H\alpha 0}/I_{H\beta 0} 10^{-C_{\lambda}(H\alpha)-(H\beta)}$, where I_0 and I denote the flux before and after extinction, and $f(\lambda)$ is the extinction curve.

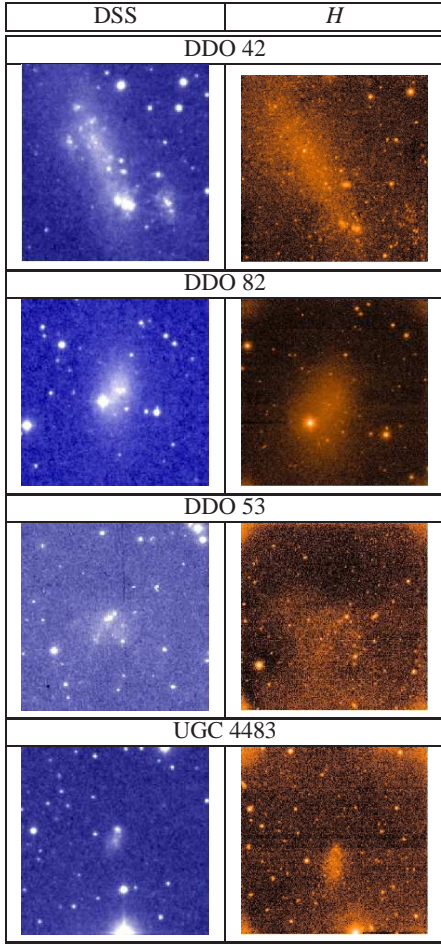


Figure 2. The NIR, H -band, morphology of the M81 group dIrrs observed at WHT with INGRID (right column) is compared to their optical appearance as seen in DSS images (left column). The galaxy luminosity decreases from top to bottom panels. In all images, North is up and East to the left, and the field of view is $\sim 6' \times 6'$ in the left column and $\sim 5' \times 5'$ in the right column.

In some cases the $H\alpha$ line profile showed more than one region: in this case the two brightest regions were extracted (see Table 4). The spectra of the brightest H II regions that enter the L-Z relation for each galaxy are shown in Fig. 3.

Full account of the data reduction is reported in Appendix A. The reddening corrected fluxes for each useful region are listed in Table 4; for the regions where $[O III]\lambda 4363$ has been detected, we list their physical parameters and abundances in Table 6.

2.2.2. M81 group

The spectra of the M81 group dwarfs were obtained with the *Kast* Double Spectrograph at the Cassegrain focus of the Shane 3m Telescope, at Lick observatory. The instrument consists of two separate spectrographs – one optimized for the red, and the other for the blue –. Dichroic beam-splitters and separate CCD detectors allow simultaneous observation. Both arms use a UV-flooded Reticon 1200 \times 400 px device, with $2.7\mu m$ pixels covering $0''.8$ on the sky; the ADC sets a maximum ADU count of 32000, with a gain of $3.8 e^-/ADU$, and the read-out noise is $6 e^-$. The CCDs have a 40% quantum efficiency at 3200\AA . We used a $1''.5$ wide slit. The observations were carried out simultaneously with the blue and the red arms, using dichroic D46. In

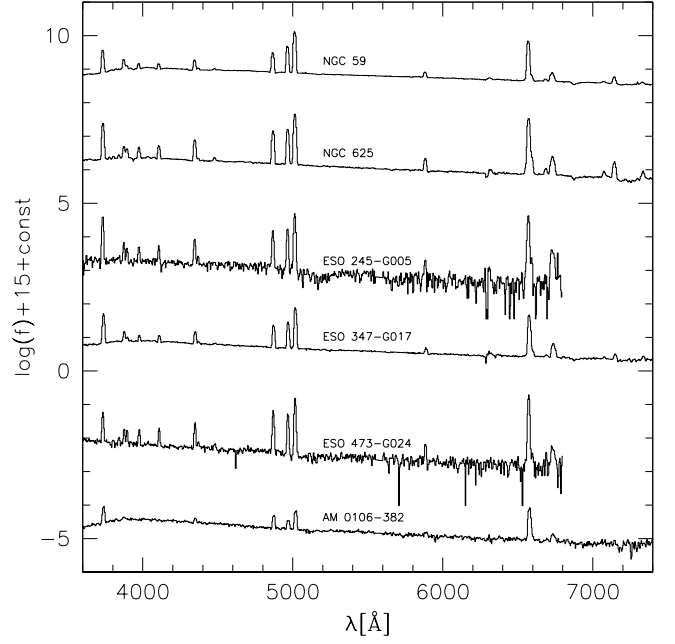


Figure 3. For each dIrr in the Sculptor group sample we show the spectrum of one of the H II regions that enter the L-Z relation. The spectra are masked near the strong night sky line $[O I]\lambda 5579$, which leads to poor sky subtraction. The reddest, noisiest, part of the spectrum is omitted for two objects. For display purposes, each flux has been multiplied by 10^{15} and a constant has been added.

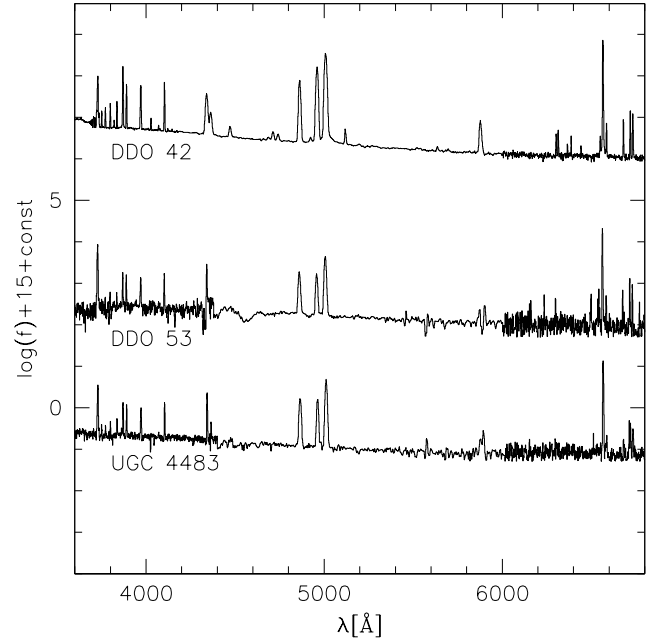


Figure 4. For three galaxies in the M81 group sample the spectrum of the target H II region is shown, with a label identifying the host galaxy. The spectra of other galaxies are of poor quality and have not been used for abundance determinations. For display purposes, each flux has been multiplied by 10^{15} and a constant has been added.

Table 5. Reddening-corrected fluxes for all H II regions in M81 group galaxies.

Ion λ [Å]	DDO 42	DDO 53	UGC 4483	Ion λ [Å]	DDO 42	DDO 53	UGC 4483
He I 3613.6	0.004 \pm 0.009	He I 4921.9	0.010 \pm 0.003
He I 3634.3	0.007 \pm 0.009	[O III] 4958.9	2.239 \pm 0.011	0.805 \pm 0.029	0.848 \pm 0.014
H19 3686.8	0.002 \pm 0.009	[O III] 5006.8	5.328 \pm 0.017	2.445 \pm 0.045	2.551 \pm 0.021
H18 3691.6	0.004 \pm 0.009	? 5118.0	0.023 \pm 0.003
H17 3697.2	0.005 \pm 0.009	[O I] 5577.3	0.041 \pm 0.014
H16 3703.9	0.012 \pm 0.009	...	0.061 \pm 0.027	^(a) 5635.0	0.005 \pm 0.004
H15 3712.0	0.010 \pm 0.009	He I 5875.7	0.107 \pm 0.007	...	0.061 \pm 0.019
S III+H14 3722.0	0.025 \pm 0.009	[O I] 6300.3	0.012 \pm 0.007
[O II] 3726.0	0.581 \pm 0.009	2.275 \pm 0.076	0.871 \pm 0.028	[S III] 6312.1	0.017 \pm 0.007
H13 3734.4	0.021 \pm 0.009	[O I] 6363.8	0.005 \pm 0.007
H12 3750.2	0.031 \pm 0.009	...	0.064 \pm 0.026	? 6386.0	0.006 \pm 0.007
H11 3770.6	0.042 \pm 0.009	...	0.072 \pm 0.026	? 6441.0	0.003 \pm 0.007
H10 3797.9	0.055 \pm 0.008	0.104 \pm 0.067	0.076 \pm 0.025	[N II] 6548.0	0.013 \pm 0.008	...	0.015 \pm 0.024
He I 3819.6	0.011 \pm 0.008	H α 6562.8	2.849 \pm 0.008	2.849 \pm 0.101	2.851 \pm 0.037
H9 3835.4	0.075 \pm 0.008	0.111 \pm 0.065	0.099 \pm 0.025	[N II] 6583.4	0.027 \pm 0.008	0.051 \pm 0.050	0.034 \pm 0.025
[Ne III] 3868.8	0.632 \pm 0.008	0.294 \pm 0.064	0.183 \pm 0.024	He I 6678.1	0.030 \pm 0.008	0.070 \pm 0.052	0.018 \pm 0.026
H8 3889.1	0.225 \pm 0.008	0.282 \pm 0.062	0.196 \pm 0.024	[S II] 6716.5	0.055 \pm 0.008	0.148 \pm 0.056	0.080 \pm 0.026
He 3970.1	0.353 \pm 0.008	0.343 \pm 0.058	0.207 \pm 0.022	[S II] 6730.8	0.045 \pm 0.008	0.104 \pm 0.056	0.059 \pm 0.026
He I 4026.2	0.018 \pm 0.007	He I 7065.3	0.031 \pm 0.010	...	0.029 \pm 0.030
[S II] 4068.6	0.006 \pm 0.007	...	0.013 \pm 0.020	[Ar III] 7135.8	0.059 \pm 0.010	0.035 \pm 0.058	0.026 \pm 0.031
[S II] 4076.4	0.001 \pm 0.007	He I 7281.3	0.004 \pm 0.010
H δ 4101.7	0.297 \pm 0.007	0.302 \pm 0.050	0.233 \pm 0.019	O II] 7319.6	0.009 \pm 0.010
He I 4120.9	0.002 \pm 0.006	O II] 7330.2	0.013 \pm 0.010
He I 4143.8	0.001 \pm 0.006	[Ar III] 7751.1	0.015 \pm 0.012
Hy 4340.5	0.536 \pm 0.008	0.470 \pm 0.035	0.419 \pm 0.015	? 8058.0	0.012 \pm 0.013
[O III] 4363.2	0.165 \pm 0.008	...	0.049 \pm 0.013	? 8083.0	0.011 \pm 0.013
He I 4471.5	0.048 \pm 0.005	Pa16 8502.5	0.003 \pm 0.014
? 4693.0	0.004 \pm 0.001	Pa15 8545.4	0.006 \pm 0.014
He I 4713.2	0.034 \pm 0.003	Pa14 8598.4	0.005 \pm 0.014
C II 4744.9	0.026 \pm 0.003	Pa13 8665.0	0.016 \pm 0.015
H β 4861.3	1.000 \pm 0.008	1.000 \pm 0.028	1.000 \pm 0.014	C H α /H β ^b	0.020 \pm 0.010	0.216 \pm 0.068	0.001 \pm 0.030

Notes: ^(a) S II λ 5640? ^(b) The reddening constant is computed by the expression: $I_{H\alpha}/I_{H\beta} = I_{H\alpha 0}/I_{H\beta 0} 10^{-C[f(H\alpha)-f(H\beta)]}$, where I_0 and I denote the flux before and after extinction, and $f(\lambda)$ is the extinction curve.

one occasion we also obtained a spectrum with the red arm alone (without dichroic) to check the flux normalization in the overlap region of the red and blue spectra. Table 3 summarizes the observations, carried out in December 2001 and January 2002. Due to poor weather conditions, and the overheads of the trial-and-error technique, only six galaxy targets were observed in three nights, of which one is the higher redshift object KDG 54.

The reduction and analysis of the spectroscopic data is similar to that of EFOSC2 (see Appendix A), although more steps are needed to correct for the large flexures and to ensure a proper normalization of the spectra in the two arms (see Appendix B). Spectra with adequate S/N ratio could be obtained for three galaxies, they are shown in Fig. 4.

The reddening corrected fluxes for each useful region are listed in Table 5, and for the regions where [O III] λ 4363 was detected, their derived physical parameters and abundances are provided in Table 6.

2.3. NIR imaging

The imaging part of the project was carried out with the 4m William Herschel Telescope (WHT) and the 3.5m New Technology Telescope (NTT). The instrument INGRID (Isaac Newton Group Red Imaging Device) was used at the former, and SOFI (Morwood et al. 1998) at the latter. Both instruments make use of 1024x1024 HgCdTe Hawaii arrays, and the chosen scales were respectively of 0''.238 px⁻¹ and 0''.288 px⁻¹.

The observations were performed with the typical pattern for infrared imaging: iterating every 1-2 minutes between the object and a nearby patch of clear sky, usually 3-5' away from the galaxy. Each image was averaged over a number of short integrations, usually 10-30 sec, to avoid saturation of the array from the combination of the sky background and any bright foreground objects. Small offsets – of order of 5-10'' – were introduced between successive object or sky images to ensure that the target was placed on different locations of the array. This helps removing cosmetic defects and improves the flat-fielding. A log of the observations is presented in Table 2 and in Table 3.

Detailed account of the data reduction and calibration is provided in Appendix C. The main steps of the NIR surface photometry are: (a) accurate flat-fielding with polynomial fitting of the background; (b) masking of foreground stars; (c) deriving the light-profile by integration in elliptical annuli. Errors on the total magnitudes have been estimated by changing the background level by $\pm 1\sigma$, integrating the two new growth curves, and then computing the difference with the magnitude obtained from the average growth curve. In turn, the r.m.s. fluctuation of the background was estimated by measuring the background itself in 10–20 independent areas. The total magnitudes of all galaxies are listed in Table 7, except for DDO 82, dropped out because no estimate of its abundance could be obtained; its magnitude is $H = 10.83 \pm 0.37$ mag.

Table 6. Physical parameters and abundances for H II regions in the dIrrs of the Sculptor and M81 groups, for which the electron temperature could be determined. The O^{++}/H^+ and S^{++}/H^+ abundances are the average of the two values obtained from the two lines of the doublet separately ($\lambda\lambda 5007, 4959$, and $\lambda\lambda 6716, 6731$, respectively)

Parameter	ESO 245-G005 external	ESO 245-G005 central	ESO 347-G017 #1	ESO 473-G024	DDO 42
T (O III) (K)	14500^{+1970}_{-2020}	14200^{+4290}_{-4680}	12660^{+933}_{-970}	14770^{+1670}_{-1690}	18500^{+548}_{-542}
$n(S II)$ (cm^{-3})	605 ± 547	674 ± 615	164 ± 100	545 ± 487	682 ± 636
O^{++}/H^+ ($\times 10^5$)	2.27 ± 0.09	7.75 ± 0.16	6.63 ± 0.24	2.84 ± 0.18	3.82 ± 0.53
O^+/H^+ ($\times 10^5$)	1.90 ± 0.96	8.67 ± 7.45	3.54 ± 1.03	1.06 ± 0.47	0.31 ± 0.06
O/H ($\times 10^5$)	4.17 ± 0.96	16.42 ± 7.45	10.17 ± 1.06	3.90 ± 0.50	4.13 ± 0.53
$12 + \log(O/H)$	7.61 ± 0.10	8.17 ± 0.21	8.00 ± 0.05	7.59 ± 0.06	7.61 ± 0.06
N^+/O^+ ($\times 10^2$)	...	2.24 ± 4.15	2.18 ± 1.62	3.30 ± 4.77	6.77 ± 5.50
$\log(N/O)$...	-1.65 ± 0.46	-1.66 ± 0.24	-1.48 ± 0.39	-1.17 ± 0.26
N/H ($\times 10^6$)	...	1.94 ± 5.27	0.77 ± 0.80	0.35 ± 0.66	0.21 ± 0.21
S^+/H^+ ($\times 10^7$)	3.29 ± 0.38	9.73 ± 3.68	5.06 ± 0.48	1.81 ± 0.52	0.72 ± 0.18
S^{++}/H^+ ($\times 10^7$)	38.1 ± 24.6	5.29 ± 2.58
ICF	1.32 ± 0.31	1.97 ± 0.24
S/H ($\times 10^6$)	5.44 ± 2.46	1.19 ± 0.26
$12 + \log(S/H)$	6.69 ± 0.21	6.06 ± 0.10
S/O ($\times 10^2$)	1.30 ± 0.89	0.29 ± 0.10
$\log(S/O)$	-1.89 ± 0.23	-2.54 ± 0.13

Parameter	NGC 625 #1	NGC 625 #2	NGC 59 #1	NGC 59 #2	UGC 4483
T (O III) (K)	10100^{+1060}_{-1220}	9400^{+678}_{-758}	10700^{+1670}_{-2020}	15200^{+5340}_{-5640}	15000^{+1890}_{-1900}
$n(S II)$ (cm^{-3})	622 ± 549	135 ± 63	736 ± 667	3120 ± 3070	2000 ± 1940
O^{++}/H^+ ($\times 10^5$)	16.42 ± 0.45	15.41 ± 0.54	19.01 ± 0.48	8.11 ± 1.69	2.92 ± 0.08
O^+/H^+ ($\times 10^5$)	7.37 ± 4.01	8.48 ± 3.04	6 ± 4.29	19.03 ± 6.93	1.21 ± 0.72
O/H ($\times 10^5$)	23.79 ± 4.04	23.89 ± 3.09	25.01 ± 4.32	27.14 ± 7.13	4.13 ± 0.72
$12 + \log(O/H)$	8.37 ± 0.07	8.37 ± 0.06	8.39 ± 0.08	8.42 ± 0.12	7.61 ± 0.08
N^+/O^+ ($\times 10^2$)	3.10 ± 4.47	...	5.12 ± 8.17
$\log(N/O)$	-1.51 ± 0.39	...	-1.29 ± 0.41
N/H ($\times 10^6$)	1.86 ± 4.01	...	0.62 ± 1.36
S^+/H^+ ($\times 10^7$)	7.49 ± 0.44	6.79 ± 0.51	7.32 ± 1.62	21.33 ± 6.80	2.34 ± 0.81
S^{++}/H^+ ($\times 10^7$)	153 ± 98	...	156 ± 139
ICF	1.43 ± 0.37	...	1.95 ± 0.86
S/H ($\times 10^6$)	23.06 ± 9.87	...	31.80 ± 14.02
$12 + \log(S/H)$	7.32 ± 0.20	...	7.46 ± 0.21
S/O ($\times 10^2$)	0.97 ± 0.58	...	1.27 ± 0.78
$\log(S/O)$	-2.01 ± 0.20	...	-1.90 ± 0.21

3. Derivation of the chemical abundances

Since the main purpose of this study is to use oxygen abundances in the search for a correlation with the galaxy luminosity, we defer a complete discussion of the elements other than oxygen to a future paper. Yet, the abundances of two other important elements (nitrogen and sulfur) have been derived as described in this section, and are listed in Table 6. The abundances have been computed with the so-called direct method (e.g. Osterbrock 1989).

The O III region electron temperatures T_e , electron densities n_e , and abundances have been computed using tasks within the NEBULAR package of IRAF. Since temperature and density cannot be derived independently, we start with suitable initial values and iterate the task TEMDEN until the values stabilize within the errors: the temperature is computed using the [O III] line ratio ($\lambda 4959 + \lambda 5007$)/ $\lambda 4363$, and the density is derived from the [S II] line ratio $\lambda 6716/\lambda 6731$. Using these values for T_e and n_e , for every ion the abundance is computed with the IONIC task, with central wavelengths, line ratios, and errors listed in Table 4 and Table 5 for the Sculptor and M81 groups, respectively. The tolerance on the central wavelength is generally taken as 1 Å, except in cases where the line is actually an unresolved doublet

or blend. This happens for the following multiplets: [O I] $\lambda 6364$ (tolerance=2 Å), [O II] $\lambda 3727$ (4 Å), [O II] $\lambda 7325$ blend (10 Å), and the [S II] $\lambda 4072$ blend (7 Å).

The total oxygen abundance is computed as $O/H = O^{++}/H^+ + O^+/H^+$, i.e. neglecting the usually small contribution from O^{+3} (Skillman & Kennicutt 1993). On the other hand, higher ionization stages of sulfur do contribute to the total abundance (Dufour et al. 1988), so an ionization correction factor (ICF) has to be computed and taken into account. This is extensively discussed in Garnett (1989), who computed a series of photoionization models and compared them with the relation $(S^+ + S^{++})/S = [1 - (O^+/O)^\alpha]^{1/\alpha}$ proposed by Stasinska (1978) with $\alpha = 3$ and French (1981) with $\alpha = 2$. Neither choice of α gives an entirely satisfactory result, however we have found that for $\alpha = 2.6$ the relation reproduces Garnett's models in the range $O^+/O > 0.2$, which corresponds to the case of all our H II regions. Thus, sulfur abundances are computed as $S/H = ICF \times (S^+ + S^{++})$, with $ICF = [1 - (1 - O^+/O)^{2.6}]^{-1/2.6}$; the correction factors are listed in Table 6. Finally nitrogen abundances are computed assuming $(N/O) = (N^+/O^+)$, and then using the nitrogen to oxygen ratio in the equation $(N/H) = (N/O) \times (O/H)$.

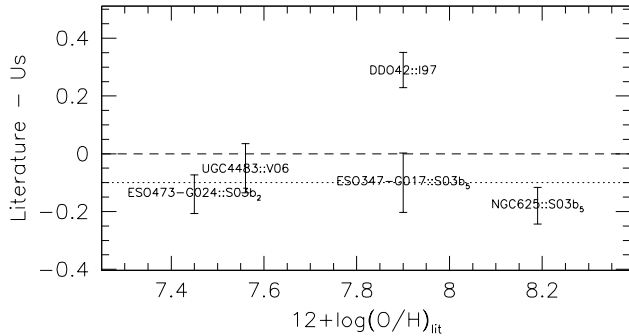


Figure 5. Comparison of our abundance determinations to literature values, for H II regions in galaxies with independent – and direct – determinations of $12 + \log(\text{O}/\text{H})$. The dotted line marks the median deviation of -0.1 dex. The galaxy name is followed by the reference acronym, and its subscript is the region number in the reference paper.

3.1. Comparison with previous abundance determinations

A summary of our measurements is given in Table 7, and, for each galaxy, the best literature direct measurement of the oxygen abundance is reported as well. If no direct measurement exists, then we list the best indirect measurement (i.e. the temperature cannot be estimated, so abundance estimates rely upon semi-empirical relations making use of different line ratios). There are five galaxies in our sample for which the abundances can be compared to values already published: this is shown in Fig. 5. There is a general agreement except for DDO 42, which exhibits an internal metallicity gradient and is discussed in more detail in Sect. 4. Excluding this galaxy, the dispersion in the value differences is only 0.06 dex. However, the median of the literature values is 0.1 dex lower than ours (dotted line in the figure). We tried to understand this discrepancy by examining NGC 625, which shows the largest difference. As a first check, we compared our fluxes to those of S03b for the same nebula in this galaxy: the two studies are fairly consistent, our fluxes being only 3% smaller on average and with a dispersion of 14%, and no trend with wavelength. The exception is the [S III] $\lambda 6312$ line, for which our flux is ~ 2 times larger than that quoted in S03b. With respect to the oxygen lines, our fluxes are 17% and 25% smaller for the [O II] $\lambda 3727$ and [O III] $\lambda 4363$ lines, respectively, while the [O III] $\lambda 4959$ and $\lambda 5007$ line fluxes are only 7% and 6% smaller, respectively. Such flux discrepancies are entirely within the errors we quote, yet they are responsible for most of the abundance differences. Indeed, using the fluxes listed in S03b we obtain $12 + \log(\text{O}/\text{H}) = 8.26$ dex for NGC 625 (region 5), so the difference is reduced from 0.18 dex to 0.07 dex, i.e. it is now within our 1σ error on the abundance.

Since the measured green [O III] line fluxes are very close to those of S03b, we discuss only the blue [O III] $\lambda 4363$ and [O II] lines here. The difference in flux for the [O II] $\lambda 3727$ line could be due to the fact that for $\lambda < 4000\text{\AA}$ the EFOSC2 response function starts dropping steadily, and large corrections have to be applied. On the other hand, comparing the response functions obtained at different epochs shows that the uncertainty on our response curve is at the level of a few 0.1%. S03b do not show their response function, but since they are using an order sorting filter with 50% cut at 3600\AA it is very likely that their correction to the [O II] line is quite large as well (almost a factor of two). In

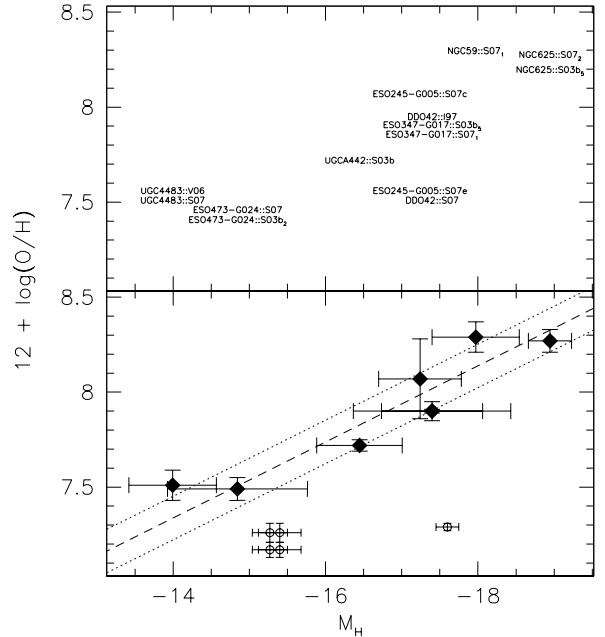


Figure 6. Metallicity of H II regions vs. absolute H luminosity of galaxies in the Sculptor and M81 groups. The upper panel shows all direct oxygen measurements listed in Table 7, while in the lower panel only selected regions are plotted with filled diamonds (see text). The dashed line is a weighted least-squares fit to the data, and the dotted lines feature the $\pm 1\sigma$ dispersion around the fit. The galaxy IDs in the upper panel are followed by the acronym of the paper where the abundances have been published (see Table 7), and the subscript is the region number in that paper. To separate the labels, small random vertical offsets have been introduced. The open circles at $M_H \sim -15.5$ represent the two components of I Zw 18 for the two distances listed in Table 7, while the open square represents SBS 0335-052.

any case, adopting the S03b [O II] line flux leads only to a minor *increase* in abundance of 0.03 dex. Most of the abundance dependence is then in the [O III] $\lambda 4363$ line, and indeed changing its flux and adopting the S03b value we get $12 + \log(\text{O}/\text{H}) = 8.19$. In this case, the flux quoted in S03b might be more reliable than ours. Indeed, we have to deblend this line from H γ , while on the spectra published by S03b the line is well separated from H γ . Since [O III] $\lambda 4363$ becomes weaker as the oxygen abundance increases – hence the temperature decreases – this could explain why the most deviant abundance value is that corresponding to NGC 625, the most metal-rich galaxy in our sample.

4. The NIR luminosity-metallicity relation

Table 7 summarizes the galaxy parameters which have been used to create the L-Z relation. Besides oxygen abundances and NIR luminosities, the table reports on distances and total extinctions in the H band, taken from Schlegel et al. (1998). Distances based on standard candles are available for only a fraction of the targets, so in most cases we have used approximate values. In particular for the Sculptor group, distances were taken from S03a (computed with the method of J98). This method relies on the recession velocity, and is claimed to provide distances within 20% of the direct measurement. The three galaxies with distances computed with the red-giant branch tip (RGBT)

Table 7. Data for the L-Z relation of Sculptor and M81 dIrrs, taken both from the literature and from the present work. The abundances, computed with the method identified in the third column, have been extracted from the publication identified by its acronym in the fourth column (see the bibliography); S08 is this paper. The abundance methods are D=direct, M=McGaugh, P=Pilyugin, and I=indirect. Notes on abundances are: (a) average of 3 regions; (b) average of two methods; (c) central region; (d) external region. Distances have been computed with the method identified in the sixth column, and have been extracted from the publication identified by its acronym in the seventh column (see the bibliography). The distance methods are J98, assuming an error of 20% and RGBT – red giant branch tip –. Total apparent H -band magnitudes are from this work, and the H -band extinctions are from Schlegel et al. (1998).

Name	12+log(O/H)	Method	Ref	D [Mpc]	Method	Ref	A _H	m _{H,tot}	M _H
Sculptor group									
ESO 347-G017	8.00 ± 0.05	D	S08#1	6.99 ± 1.40	J98	S03a	0.010	11.79 ± 0.50	−17.40 ± 0.66
	7.87 ± 0.20	P	S08#1						
	7.90 ± 0.09	D	S03b#5						
UGCA 442	S08	4.27 ± 0.52	RGBT	K03	0.010	11.70 ± 0.50	−16.45 ± 0.56
	7.72 ± 0.03	D	S03b						
ESO 348-G009	S08	6.52 ± 1.30	J98	S03a	0.008	12.80 ± 0.61	−16.24 ± 0.75
	7.89 ± 0.03	M	S03b, L03						
	8.11 ± 0.05	P	S03b, L03						
NGC 59	8.39 ± 0.08	D	S08#1	4.39 ± 0.87	J98	S03a	0.012	10.21 ± 0.37	−17.97 ± 0.57
	7.74 ± 0.20	P	S08#1						
ESO 473-G024	7.59 ± 0.06	D	S08	5.94 ± 1.19	J98	S03a	0.011	13.99 ± 0.81	−14.85 ± 0.92
	7.45 ± 0.20	P	S08						
	7.45 ± 0.03	D	S03b#2						
AM 0106-382	7.74 ± 0.20	P	S08	6.13 ± 1.23	J98	S03a	0.007	14.38 ± 0.65	−14.52 ± 0.78
	7.58 ± 0.04	M	L03(a)						
	7.62 ± 0.08	P	L03(a)						
NGC 625	8.37 ± 0.06	D	S08#2	3.89 ± 0.22	RGBT	C03	0.010	9.01 ± 0.26	−18.95 ± 0.28
	7.69 ± 0.20	P	S08#2						
	8.19 ± 0.02	D	S03b#5						
ESO 245-G005	8.17 ± 0.21	D	S08(c)	4.43 ± 0.45	RGBT	K03	0.009	10.99 ± 0.50	−17.24 ± 0.54
	7.61 ± 0.10	D	S08(d)						
	7.96 ± 0.20	P	S08						
	7.65–8.20	M	M96, H03						
M81 group									
DDO 42	7.61 ± 0.06	D	S08	3.20 ± 0.41	RGBT	K02	0.021	10.13 ± 1.00	−17.40 ± 1.03
	7.73 ± 0.20	P	S08						
	7.9 ± 0.01	D	I97						
DDO 53	7.83 ± 0.20	P	S08	3.57 ± 0.25	RGBT	K02	0.021	12.64 ± 1.30	−15.14 ± 1.31
	8.00 ± 0.23	i	HH99(b)						
UGC 4483	7.61 ± 0.08	D	S08	3.40 ± 0.20	RGBT	IT02	0.020	13.68 ± 0.56	−13.99 ± 0.57
	7.43 ± 0.20	P	S08						
	7.56 ± 0.03	D	V06						

Table 8. Abundances and NIR luminosities for the fiducial sample of galaxies. Distances are expressed in Mpc, and columns 6 and 7 indicate the method used to compute the distance, and its reference. Our abundances have been corrected by -0.1 dex. For comparison we add also I Zw 18 ($H = 16.03 \pm 0.15$; Thuan 1983) and SBS 0335-052 ($H = 16.09 \pm 0.03$, $15''$ aperture; Vanzani et al. 2000)

Galaxy	Group	12 + log (O/H)	Ref.	Distance	Met.	Ref.	M_H
ESO 347-G017	Scl	7.90 ± 0.05	S08#1	6.99 ± 1.40	J98	S03a	-17.40 ± 0.66
NGC 59	Scl	8.29 ± 0.08	S08#1	4.39 ± 0.87	J98	S03a	-17.97 ± 0.57
ESO 473-G024	Scl	7.49 ± 0.06	S08	5.94 ± 1.19	J98	S03a	-14.85 ± 0.92
NGC 625	Scl	8.27 ± 0.06	S08#2	3.89 ± 0.22	RGBT	C03	-18.95 ± 0.28
ESO 245-G005	Scl	8.07 ± 0.21	S08c	4.43 ± 0.45	RGBT	K03	-17.24 ± 0.54
UGC 4483	M81	7.51 ± 0.08	S08	3.40 ± 0.20	RGBT	IT02	-13.99 ± 0.57
UGCA 442	M81	7.72 ± 0.03	S03b	4.27 ± 0.52	RGBT	K03	-16.45 ± 0.56
DDO 42	M81	7.90 ± 0.01	I97	3.20 ± 0.41	RGBT	K02	-17.40 ± 1.03
I Zw 18 – SE	...	7.26 ± 0.05	SK03	18.2 ± 1.5	RGBT	A08	-15.27 ± 0.23
I Zw 18 – NW	...	7.17 ± 0.04	SK03	19.3 ± 2.3	Ceph.	A08	-15.40 ± 0.28
SBS 0335-052	...	7.29 ± 0.02	I06	54.8 ± 3.8	Hub.fl.	NED	-17.60 ± 0.15

luminosity enable a test of this method: they are UGCA 442, NGC 625, and ESO 245-G005, and their distances obtained with the J98 method are respectively 18% smaller, 10% larger, and 15% smaller than the ones quoted in Table 7. For the M81 group, all four galaxies have distances obtained with the RGBT technique, and the DDO 42 distance has been measured by both Karachentsev et al. (2002; K02) and Thuan & Izotov (2005; TI05). Although the TI05 distance (3.42 ± 0.15 Mpc) has a smaller formal error, we adopt the K02 distance, as, doing so, we have consistent distances for three galaxies in our sample.

All galaxies having direct abundance determinations are plotted in the upper panel of Fig. 6. A correction of -0.1 dex has been applied to our data, in order to be consistent with Skillman et al. (2003b). There appears an obvious trend of increasing metallicity with H luminosity, except for the two galaxies at $12 + \log(\text{O}/\text{H}) \approx 7.5$ and $M_H \approx -17$ mag. These are ESO 245-G005 and DDO 42: the latter has an independent oxygen abundance from Izotov et al. (1997), which is higher than our value and consistent with that of ESO 347-G017 at comparable luminosity. Since the work of Roy et al. (1996), it is known that DDO 42 displays a range of abundances consistent with a shallow gradient, so our low value probably reflects the external location of our target H II region. In the following we will then adopt the Izotov et al. value which corresponds to a central region, and we note that a key point in the definition of an L-Z relation is that, for each galaxy, *regions close to their centers should be selected*. The case of ESO 245-G005 is similar to that of DDO 42: in this galaxy, we measured both an external and a central region, finding an abundance difference of ≈ 0.5 dex. Our direct abundances (the first ones for this galaxy) confirm the metallicity gradient found by Miller (1996; M96) with an indirect method: our range is $12 + \log(\text{O}/\text{H}) = 7.61$ to 8.17 while M96 finds a range 7.65 to 8.20 . A similar result has been obtained by Hidalgo-Gómez et al. (2003). Again, we adopt the central abundance as the reference for this galaxy.

From the sample plotted in the upper panel of Fig. 6 we extracted the galaxies listed in Table 8, which are the fiducial objects defining our L-Z relation. Whenever possible we select abundances from our work, except for two galaxies: UGCA 442 was not observed spectroscopically, and our observed DDO 42 region was excluded for the reason discussed above. Our fiducial L-Z relation is plotted in the lower panel of Fig. 6. The obvious abundance trend with luminosity is confirmed by a correlation coefficient $r = -0.93$: a weighted least-squares fit yields the following relation:

$$12 + \log(\text{O}/\text{H}) = -0.20 \pm 0.03 M_H + 4.54 \pm 0.49$$

with a dispersion of 0.11 dex around the fit.

Table 8 includes also data for the blue-compact dwarf (BCD) galaxies I Zw 18 and SBS 0335-052. These are possibly the most metal-poor galaxies in the local Universe, so it is worthwhile to see how they compare with our sample of dwarf irregular galaxies. This is done in Fig. 6, where the two objects are plotted with open symbols. They fall outside the trend defined by dIrr galaxies, in the sense that their oxygen abundances are too low for their luminosities. There might be several explanations for this fact: the first possibility is that the gas enrichment of BCD galaxies is slower than that of dIrr galaxies, either because they produce less metals per stellar generation, or because they lose metals into the IGM more easily. So, as the luminosity of a BCD increases, its oxygen abundance does not increase as much as that of a dIrr of comparable mass. A second possibility is that we are not measuring the central abundances of the two BCDs.

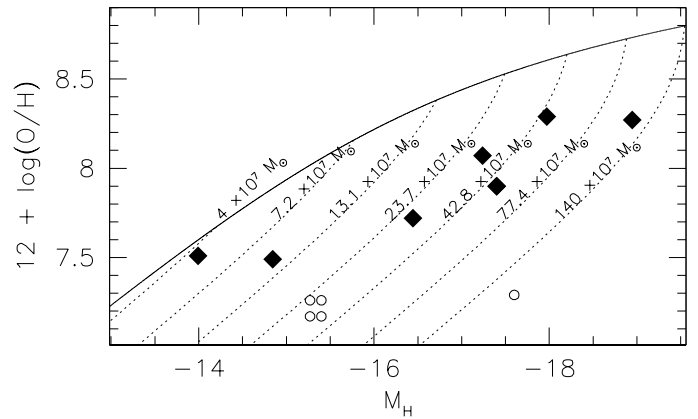


Figure 7. Comparison of the luminosities and abundances of our fiducial galaxies (filled diamonds) with the predictions of a set of closed-box models of increasing total masses (dotted line curves). For each model the evolution has been truncated when the remaining gas mass drops below $3 \times 10^7 M_\odot$, and the sequence of the end-points is outlined by the solid curve. The open symbols are the same as in Fig. 6.

We have shown above that gradients as large as 0.5 dex are detected in dwarf galaxies, so the low abundance of the H II regions in I Zw 18 and SBS 0335-052 might be explained by their non-central location. Indeed the H I maps presented in van Zee et al. (1998) and Hirashita et al. (2002), and compared to the optical and $\text{H}\alpha$ maps, show that the star forming regions are slightly off-center. However a counter-argument for I Zw 18 is that the galaxy is too small to have appreciable metallicity gradients. Finally in the case of SBS 0335-052, one might think that its distance is overestimated: if the distance were ~ 4 times smaller, then its luminosity would agree with the faintest objects in our sample. However at the relatively large recession velocity of the galaxy ($\sim 4000 \text{ km sec}^{-1}$) peculiar motions cannot induce such a factor of four uncertainty in the distance (e.g., Tonry 2000). The conclusion is then that these two BCD galaxies must have had different evolutionary paths than dIrr galaxies.

This remains true even when the two galaxies are compared to the general population of BCDs. Shi et al. (2005) have shown that the L-Z relation of BCD galaxies is similar to that of dIrr galaxies, so at the luminosity of I Zw 18 and SBS 0335-052 a typical BCD has higher oxygen abundances than these two objects. On the other hand the Shi et al. L-Z relation shows a very large scatter: this is not quantified by the authors, but in their Fig. 3 one can see object-to-object abundance differences of up to 1 dex. Shi et al. propose that the scatter might be due to differences in SFH or the evolutionary status of the current starburst, or to different starburst-driven outflows or gas infall rates. The abundances of I Zw 18 and SBS 0335-052 are then particularly low, but still compatible with those of BCDs in general, and could be due to one of these processes.

5. Discussion

5.1. Origin of the luminosity-metallicity relation

As recalled in the introduction, in the case of dE/dSph galaxies the L-Z relation is interpreted in the scenario of mass-loss through galactic winds. The gas escapes more easily from low mass galaxies, so their chemical evolution is truncated before that of more massive galaxies. Some previous studies have pro-

posed that dSphs and dIrrs share the same L-Z relation, thus extending the mass-loss scenario to irregulars (e.g. Skillman, Kennicutt, & Hodge 1989). However, recently it has been shown that the abundances of dIrrs are lower than those of dSphs of comparable luminosity, whether we consider their gas content (e.g. Mateo 1998) or their RGB stars (e.g. Grebel 2004). Therefore, if we want to retain the mass-loss scenario for both classes of dwarfs, then we must assume not only that this process leaves behind an L-Z relation after the evolution has stopped (dSph), but also that it induces a (possibly different) relation very early in the history of galaxies (dIrr), and is able to maintain it throughout their lives.

More input on the issue of the chemical evolution of dIrrs has been provided recently by Skillman et al. (2003b) and Pilyugin et al. (2004). Both studies conclude that the chemical evolution of dIrrs can be approximated by a closed-box, provided that an effective oxygen yield $\approx 1/3$ of the theoretical value (e.g., Maeder 1992) is adopted. A low yield can be the signature of gas exchange with the environment, and this is indeed observed in a few cases, as discussed in the introduction. If this conclusion is valid, then it is hard to imagine how mass-loss can produce the L-Z relation, because the galaxy mass is not a parameter of the closed-box model. Conversely, one would expect that the effective yield does depend on the mass of the galaxy, since the efficiency of mass-loss via galactic winds should depend on the depth of the potential well. Note also that Lee et al. (2006) have found a few dwarf galaxies with large yields, a result difficult to reconcile with the galactic wind hypothesis. In conclusion, there does not appear to be any obvious interpretation of the observational facts and the situation remains confusing.

Yet, pushing further the hypothesis of a low and universal yield, we can gain some insight by looking at the dotted curves in Fig. 7, which are in fact closed-box models computed with constant yield $p_{(\text{O}/\text{H})} = 1.6 \times 10^{-4}$, and total masses $m_{\text{tot}} = m_{\text{gas}} + m_{\text{stars}}$ varying between $4 \times 10^7 M_{\odot}$ and $1.4 \times 10^9 M_{\odot}$. We also assumed $M/L_H = 1.2$ (typical of a globular cluster-like population, e.g. Bruzual & Charlot 2003), and $M_{H,\odot} = 3.1$ mag (*Astrophysical Quantities*); the only parameter varying along a track is the gas mass fraction $\mu = m_{\text{gas}}/m_{\text{tot}}$. If one assumes that all galaxies were born at the same time, then this plot is telling us that more massive galaxies evolve faster along their tracks, i.e. $d\mu/dt$ is larger for more massive galaxies. If the galaxies were formed at different times, then larger galaxies had more time to build up their metals. Skillman et al. (2003a) computed SFRs for the Sculptor group galaxies: if their data are plotted in the form $d\mu/dt = \text{SFR}/(m_{\text{gas}} + m_{\text{stars}})$ vs. $(m_{\text{gas}} + m_{\text{stars}})$, then a general trend of $d\mu/dt$ increasing with total mass can be seen. This confirms that larger galaxies are more effective in converting their gas into stars.

The conclusion is that, while a galaxy is still evolving (such as a dIrr) the L-Z relation could be a combined effect of mass-loss and of more efficient gas processing. A similar conclusion was reached by Pilyugin & Ferrini (2000): according to them, the L-Z relation is a combined effect of smaller gas-loss and higher astration level as the mass increases. Another prediction of this scenario is that the slope of the L-Z relation should increase with time, and the effect would be even larger if the gas is removed at earlier stages in smaller galaxies. The reason why astration becomes more efficient as the galaxy mass increases, remains to be understood. On the other hand, we should recall that one of the most accepted facts about star formation is that it depends on the gas density (Schmidt 1959), a conclusion also suggested by recent simulations (e.g., Chiosi & Carraro 2002).

So it might be that as its mass increases, a galaxy becomes more effective at compressing its gas.

The open symbols in Fig. 7 represent again the two BCD galaxies I Zw 18 and SBS 0335-052. In Sect. 4 we concluded that they do not follow the trend defined by dIrr galaxies because their chemical evolution must be different. Our simplified approach would tell us that I Zw 18 is on the track of a $\sim 3 \times 10^8 M_{\odot}$ galaxy, while SBS 0335-052 is on that of a $\sim 2 \times 10^9 M_{\odot}$ object, and that – compared to a dIrr of similar total mass – they did not convert much of their gas into stars, thus having very low metallicities. However it is also possible that their evolutionary paths are different: for example their compactness might imply higher densities, hence SFRs, which in turn would trigger more powerful stellar winds and remove metals more easily than in dIrr galaxies. Or they might be unusually young.

The closed-box scenario itself does not make any prediction about the final abundance a galaxy can reach: actually it predicts arbitrarily large values of Z as the gas mass fraction tends to zero, since $Z = p \ln(1/\mu)$ (Searle & Sargent 1972). However, if we assume that the mass of each new generation of stars, m_{SF} , is roughly constant, then the maximum metallicity we can measure will be $Z_{\text{max}} = p \ln(m_{\text{tot}}/m_{\text{SF}}) \propto p \ln m_{\text{tot}}$, i.e. it will be proportional to the mass of the galaxy. This is shown in Fig. 7, where we assumed $m_{\text{SF}} = 3 \times 10^7 M_{\odot}$, a mass of stars that can be created in $\sim 10^8$ yr for a typical SFR $\sim 0.1 M_{\odot} \text{yr}^{-1}$. This formulation seems to provide a natural upper limit to the measurable metallicities, and it works even for large galaxy masses. Indeed, the dotted line in the top panel of Fig. 9 represents the same relation extended to $m_{\text{tot}} = 2 \times 10^{11} M_{\odot}$, and with the exception of a couple of objects, the metallicities of star-forming galaxies are always lower than this limit. It is quite surprising that an upper limit to the metallicity is provided by such a simple expression, as it is an oversimplification of galactic chemical evolution. Still, it might suggest that a characteristic mass is involved in the star formation process.

5.2. Comparison with other galaxies

The literature offers only a few O/H measurements for galaxies as faint as those in our sample, so a direct consistency check of our results is not possible. However, one can find a few dIrrs with oxygen abundances and total infrared magnitudes allowing us to verify our relation statistically.

In order to minimize any systematic errors, we limited ourselves to using the infrared magnitudes from three sources: the 2MASS Extended Source Catalog (Jarrett et al. 2000), Cairós et al. (2003), and Hunter & Elmegreen (2006). No corrections for the different filter systems were applied. Furthermore, we used only oxygen abundances derived with the temperature sensitive method. The only exception is DDO 43, where $T_e = 10000$ K was assumed instead of being measured. Finally, the distances for galaxies closer than ~ 10 Mpc were based on direct measurements rather than on the Hubble flow. The data used for the comparison are listed in Table 9. More than one O/H measurement per galaxy is listed, whenever available. Radial velocities are taken from the NASA extragalactic database. If the literature sources do not list the O/H uncertainty, 0.1 dex was adopted. The distances flagged with “h” are based on the Hubble flow ($H_0 = 72 \text{ km s}^{-1} \text{ Mpc}^{-1}$). The H -band extinction A_H has been taken from Schlegel et al. (1998). The table data are presented in graphical form in Fig. 8 and compared to our L-Z relation. It appears that the properties of our targets, dIrrs in the Sculptor and M81 groups, are generally similar to those of nearby dIrr galaxies, but the L-Z relations yielded by the two sets of data are

Table 9. A compilation of luminosities and abundances for a sample of nearby dwarf star-forming galaxies. The abundances listed in column 6 have been taken from the publication the number of which is given in column 8 and have been computed with the method identified in column 7: 1 = direct method but temperature not computed, assumed $T_e = 10,000$ K; 2 = direct method; 3 = unknown. The publication numbers correspond to the following papers: (1) Hunter & Hoffman 1999; (2) Hidalgo-Gómez & Olofsson (2002); (3) Vigroux et al. (1987); (4) Storch-Bergmann et al. (1994); (5) Martin (1997); (6) Kobulnicky & Skillman (1998); (7) average $\pm 1\sigma$ of abundances from the following papers: Izotov & Thuan (2004), Hunter & Hoffman (1999), Thuan & Izotov (2005), Alloin et al. (1979), Shi et al. (2005); (8) Izotov & Thuan (1998); (9) Shi et al. (2005); (10) Thuan & Izotov (2005); (11) van Zee, Haynes, & Salzer (1997); (12) Izotov & Thuan (1998); (13) Izotov & Thuan (1997). Most distances were taken from Hunter & Elmegreen (2006, HE06); in column 10 the label ‘h’ means that these authors computed the distance from the recession velocity, while a number identifies their source publication for the distance. If no distance is given in HE06, then we derived it using the NED velocity and $H_0 = 72 \text{ km sec}^{-1} \text{ Mpc}^{-1}$. Finally the DDO 43 distance is from Sharina (2004, private communication; cited in Karachentsev et al. 2004).

Name	Alt. name	R.A. J2000	Dec.	v_r (NED) [km sec $^{-1}$]	12+log(O/H)	M	Ref.	D [Mpc]	source of D	A_{tot} [mag]	H_{tot} [mag]
MRK 600		02:51:04.6	+04:27:14	1008 ± 1	7.83 ± 0.01	2	12	15.7	h	0.038	14.38 ± 0.19
NGG 1156		02:59:42.2	+25:14:14	375 ± 1	$8.23 \pm \dots$	3	3	7.8	25	0.129	9.83 ± 0.01
NGG 1569		04:30:49.0	+64:50:53	-104 ± 4	$8.37 \pm \dots$	2	4	2.5	41	0.403	9.40 ± 0.02
DDO 43	UGC 03860	07:28:17.4	+40:46:11	354 ± 1	8.30 ± 0.09	1	1	7.8	rg	0.034	13.00 ± 0.17
Haro 23	UGCA 201	10:06:18.1	+28:56:40	1363 ± 7	$8.35 \pm \dots$	2	7	20.2	h	0.014	11.77 ± 0.13
MRK 33	UGC 05720	10:32:31.9	+54:24:04	1430 ± 4	$8.35 \pm \dots$	2	9	...	n	0.007	10.70 ± 0.04
											10.84 ± 0.03
Haro 3	NGG 3353	10:45:22.4	+55:57:37	944 ± 5	8.3 ± 0.10	2	7	15.5	h	0.004	10.71 ± 0.03
											10.83 ± 0.02
											10.74 ± 0.06
Haro 4	UGCA 225	11:04:58.5	+29:08:22	646 ± 5	7.81 ± 0.02	2	8	9.5	h	0.017	14.03 ± 0.03
											13.75 ± 0.36
MRK 178	UGC 06541	11:33:28.9	+49:14:14	250 ± 1	7.93 ± 0.02	2	10	3.9	27	0.010	12.47 ± 0.15
NGG 3738		11:35:48.8	+54:31:26	229 ± 4	8.23 ± 0.01	2	5	4.9	27	0.006	9.63 ± 0.04
MRK 1307	UGC 06850	11:52:37.3	-02:28:10	1055 ± 12	7.95 ± 0.01	2	8	...	n	0.011	12.87 ± 0.02
NGG 4214		12:15:39.2	+36:19:37	291 ± 3	8.25 ± 0.05	2	6	2.9	33	0.013	8.26 ± 0.03
Haro 8	UGC 07354	12:19:09.9	+03:51:21	1526 ± 4	$8.12 \pm \dots$	2	9	22.2	h	0.010	11.97 ± 0.14
Haro 29	UGCA 281	12:26:16.0	+48:29:37	281 ± 4	7.82 ± 0.01	2	10	5.4	h	0.009	13.54 ± 0.22
								4.72	100		
LeoI HH	DDO 168	13:14:27.9	+45:55:09	192 ± 1	7.5 ± 0.20	2	2	3.5	h	0.009	11.91 ± 0.12
								4.33	101		
Haro 38	UGC 08578	13:35:35.6	+29:13:01	853 ± 7	$8.02 \pm \dots$	2	9	13.7	h	0.007	14.03 ± 0.17
Haro 43		14:36:08.8	+28:26:59	1912 ± 10	8.17 ± 0.10	2	11	30.5	h	0.011	13.66 ± 0.17
MRK 829	UGC 09560	14:50:56.5	+35:34:18	1180 ± 2	$7.69 \pm \dots$	2	9	...	n	0.007	13.07 ± 0.08
											13.05 ± 0.04
II Zw 71	UGC 09562	14:51:14.4s	+35:32:32	1292 ± 18	$8.24 \pm \dots$	2	9	...	n	0.007	11.89 ± 0.05
											12.14 ± 0.03
MRK 487	UGCA 410	15:37:04.2s	+55:15:48	665 ± 7	8.10 ± 0.04	2	13	...	n	0.008	13.35 ± 0.11
											13.25 ± 0.03
MRK 297	NGC 6052	16:05:12.9s	+20:32:32	4716 ± 4	$8.34 \pm \dots$	2	9	...	n	0.044	10.92 ± 0.06

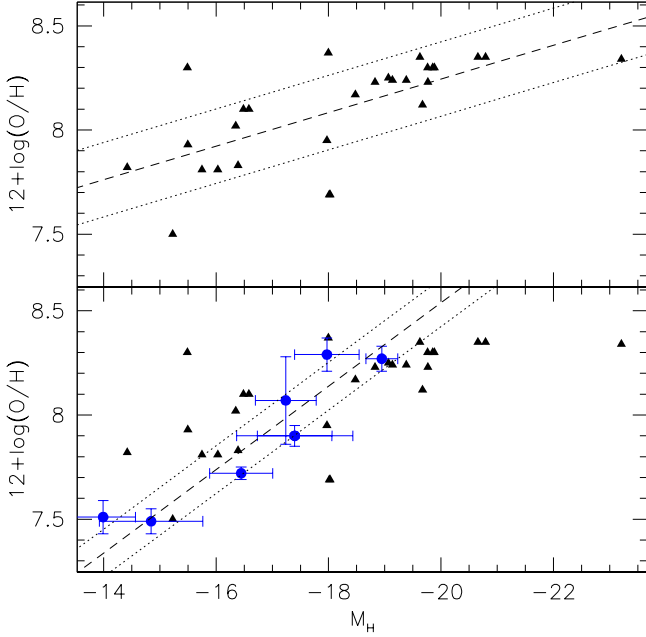


Figure 8. Abundance vs. absolute H luminosity for galaxies with data taken from the literature (filled triangles) and for our targets (filled circles). In the upper panel, the dashed line is an unweighted fit to the literature data, while our fiducial relation is shown in the lower panel. In both panels dotted lines outline the r.m.s. dispersion around the fit.

radically different. The slope of an L-Z relation based on literature data is 2.5 times smaller than the one we obtain (-0.08 ± 0.02 vs. -0.20 ± 0.03), and its dispersion is 0.18 dex, i.e. 58% larger than the scatter around our relation (0.11 dex).

The large scatter in the literature data might be ascribed to the uncertain distances, and it is also likely related to the random location of the H II regions considered inside each galaxy. Moreover, this large scatter seems to affect faint galaxies more than luminous ones, since all objects brighter than $M_H \approx -18$ exhibit a smaller scatter. Note that the literature compilation includes galaxies in diverse environments, another factor which might account for the larger spread in the literature L-Z relation in comparison with our L-Z relation for the group galaxies.

Finally, although we tried to use a sample that is as homogeneous as possible, and the method for the abundance calculation is formally the same in all these works, yet systematic differences are still possible (as demonstrated in Sect. 3.1), and they can explain part of the scatter. A detailed discussion of all the single galaxies contained in Table 9 is beyond the scope of this paper, but the conclusion is clear: any quantitative interpretation of the L-Z relation based on literature data should be performed with great caution. However, this conclusion might be revised as more and more large and homogeneous data samples appear in the literature.

5.3. A dwarf vs. giant galaxy dichotomy?

The unique study of the L-Z relation for giant galaxies that includes NIR, H -band magnitudes is that by Salzer et al. (2005; hereafter S05). They obtained spectra of emission-line galaxies in fixed apertures of $1''.5$ or $2''$, and computed oxygen abundances with a reduced number of emission lines, because of the

limited spectral coverage of their data: using additional spectra, they first derived metallicities for a subsample of galaxies using both the direct and the empirical methods, and then calibrated them against $[\text{N II}]\lambda 6583/\text{H}\alpha$ and $[\text{O III}]\lambda 5007/\text{H}\beta$. The empirical method they used is the Pilyugin (2000; P00) calibration for the lower branch of the $12 + \log(\text{O}/\text{H})$ vs. R_{23} relation, and three calibrations for the upper branch: Edmunds & Pagel (1984; EP), Kennicutt, Bresolin, & Garnett (2003; KBG), and Tremonti et al. (2004). In Fig. 9 we have plotted our data together with Salzer’s et al. data. The figure reveals that the scatter in the L-Z relation for giant galaxies is very large, compared to that of our dIrrs, perhaps due to fixed-aperture effects and uncertainties specific to the empirical methods (see also the discussion in S05). The straight lines in the upper panel are the fits obtained by S05 and by us: taken at face value, this plot would suggest a well-defined offset between the L-Z relation of giants and dwarfs. The slope of the S05 L-Z relation is in fact close to what we find for dwarfs alone, namely -0.215 ± 0.003 and -0.201 ± 0.004 for abundances obtained with the EP and KBG calibrations, respectively. Finally, to be consistent with S05, in the central panel we have plotted our abundances computed with the same P00 calibration of the empirical method, allowing two galaxies to be added (see abundances identified by “P” in Table 7). The offset between galaxies in the two mass ranges seems to disappear: it is replaced by what looks like different L-Z relations for dwarf and giant galaxies, with a separation at $M_H \approx -20$. A fit to S05 galaxies fainter than this limit yields the dotted line shown in the panel, while the solid line is a fit to our dwarfs. The two relations have a similar slope, and a ~ 0.3 dex offset, with the dwarfs of our sample being on average more metal poor than those of S05. This might result from the two-step calibration of S05, which introduces additional uncertainties in the empirical method – a method which, in any case, does not guarantee abundance precisions better than 0.2 dex. The most important thing to notice, however, is that extremely different L-Z relations are obtained for the dwarfs of our sample, if one uses abundances computed by the two methods, direct or empirical. The solid line in the upper panel of Fig. 9 (corresponding to direct abundances in the region of dwarf galaxies) has a slope of $-0.05 \text{ dex mag}^{-1}$ and an r.m.s. dispersion around this fit of 0.14 dex. The scatter is larger, and the slope is four times smaller when empirical abundances are used for the same sample of dwarfs (central panel). Striving for abundances obtained with the direct method requires a much larger observational effort, but the effort is wholly justified by the better constraints it provides on galaxy evolution.

Interestingly, using direct abundances from the literature yields an L-Z relation similar to that obtained by fitting the S05 dwarfs. This can be seen by comparing the solid line in the bottom panel of Fig. 9, to the dotted line in the central panel. The zero points are similar, and the two slopes are $-0.08 \pm 0.02 \text{ dex mag}^{-1}$ and $-0.04 \pm 0.02 \text{ dex mag}^{-1}$, respectively. The conclusion is that the use of direct abundances is not a sufficient condition: distances must be known with great accuracy as well. In that respect, let us point out that selecting a sample of dIrr galaxies in groups has been a winning strategy. Even assuming just an average distance for all galaxies in a group has allowed us to obtain essentially the same L-Z relation (Saviane et al. 2004, 2005).

The question of a dwarf-giant dichotomy is then open: moving from the empirical to the direct abundances, the L-Z relation for dwarfs becomes much better defined, parallel to the one obtained for more massive galaxies, and with a substantial offset. It remains to be seen what would happen to the L-Z relation of giant galaxies if one uses direct abundances: an impor-

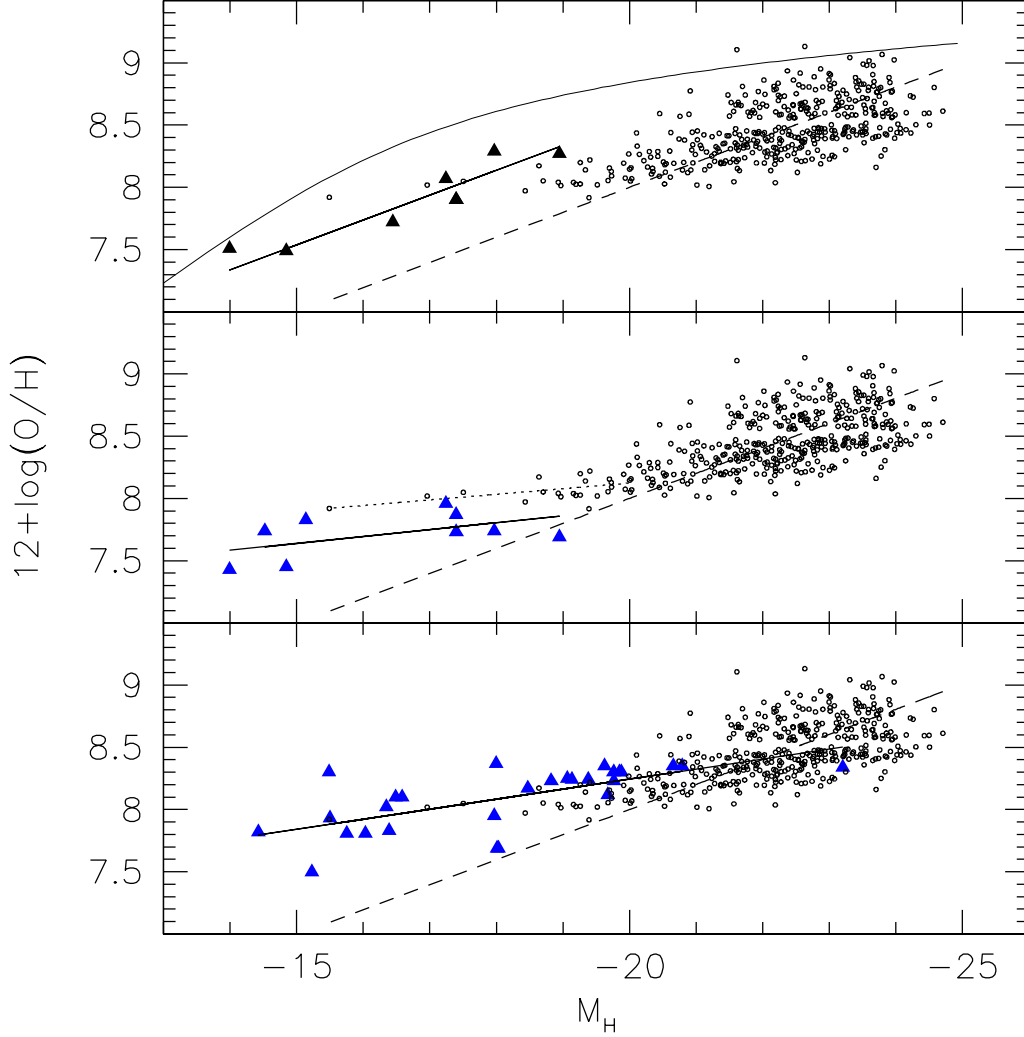


Figure 9. Oxygen abundances vs. H luminosity for the Salzer et al. (2005) emission-line galaxies (KBG calibration), our dIrrs, and data compiled from the literature. In all panels the dashed line is the fit obtained by Salzer et al. to their data points (small open circles). In the top panel, the thin solid line is the same curve as that shown in Fig. 7, while the filled triangles and solid line correspond to our fiducial L-Z relation. In the central panel, the dotted line is a weighted fit to Salzer et al. galaxies fainter than $M_H = -20$, while the filled triangles and solid line relate to our L-Z relation obtained using abundances re-computed by us with the empirical, indirect method. In the bottom panel, we show the L-Z relation from literature data (filled triangles and solid line).

tant extension of this project would be to measure direct abundances for at least some of the S05 galaxies, and check whether the observed offset is confirmed. Since the S05 sample includes star-forming galaxies, one might suspect that some of the giant galaxies are shifted in luminosity because of the presence of a star-burst: however, Lee et al. (2004) have found that this shift is a few tenths of magnitude in the B -band, compared to quiescent galaxies (however see also Bica et al. 1990). We expect that the effect in the IR must be even lower, and certainly not comparable to the ~ 2 magnitudes we observe.

A dwarf-giant galaxy dichotomy has been discussed, e.g., in Garnett (2002; hereafter G02), where the trend of effective yields $y_{\text{eff}} = Z / \ln(\mu^{-1})$ vs. galaxy luminosity or rotational velocity is studied. It is shown that dwarf galaxies (those with $v_{\text{rot}} \lesssim 100 \text{ km s}^{-1}$) have lower effective yields than massive spiral galaxies, which is interpreted as due to gas outflows in dwarfs. A similar conclusion has been reached by Tremonti et al. (2004).

In G02 the stellar mass that enters the gas mass fraction μ was computed from blue luminosities, assuming a color- M/L relation. Since more accurate stellar masses can be computed with NIR luminosities, the availability for massive spiral galaxies of abundances obtained with temperature-sensitive methods would allow more accurate effective yields to be computed as well, and therefore to update the G02 study. In particular it would be interesting to check whether indeed dwarf galaxies can lose up to 90% of their metals and be the main source of enrichment of the inter-galactic medium.

6. Summary and conclusions

We have measured oxygen abundances in H II regions located inside a number of dIrr galaxies, belonging to the nearby Sculptor and M81 groups. The abundances were measured with the temperature-sensitive (direct) method, based on the ratio of the

auroral line [O III] λ 4363 to the nebular lines [O III] λ 4959, 5007, and were complemented by direct abundances from the literature for two additional galaxies. The weak [O III] λ 4363 line could be measured in H II regions belonging to five galaxies of the Sculptor group and two galaxies of the M81 group. Metallicity gradients were detected in ESO 245-G005 and DDO 42, confirming earlier findings, so only the central highest-metallicity regions were considered for the derivation of the luminosity-metallicity relation. This forced us to discard our DDO 42 measurement, and adopt a literature value. Our fiducial sample then includes six dIrr galaxies of the Sculptor group and two galaxies of the M81 group.

For these eight galaxies we have obtained deep NIR, H -band, imaging which allowed us to perform surface photometry and compute their total luminosities. Thanks to the availability of distances with $\leq 15\%$ errors, the galaxies could be placed in the $12 + \log(\text{O}/\text{H})$ vs. M_H diagram, revealing a clear L-Z relation with a small 0.11 dex scatter around the average trend. The scatter is smaller than that of relations obtained at optical wavelengths (e.g. 0.161 dex using B -band data, Lee et al. 2006), and is comparable to the one obtained by Lee et al. (2006) with their MIR [4.5 μ m]-band data (0.12 dex). Assuming the existence of a fundamental mass-metallicity relation, the improved definition of the L-Z relation at NIR luminosities must be due to the fact that it better traces the underlying relation with mass, since the NIR mass-to-light ratio is more sensitive to the *integrated* star formation history of a galaxy. On the contrary, the blue mass-to-light ratio is more sensitive to the instantaneous SFR, which has a large galaxy-to-galaxy scatter (Saviane et al. 2004; Salzer et al. 2005).

Our work and that of Lee et al. (2006) are the ones that managed to obtain the best defined L-Z relation, and as an additional advantage, our standard NIR band allows an easy comparison to other relations obtained in independent studies. Indeed we compared our relation to that of Salzer et al. (2005), who are the only authors providing an H -band relation, at the same time extending it to giant galaxies. Unfortunately a direct comparison with our accurate abundances is not possible, since the abundances of S05 are obtained with the so-called strong-line method (indirect or empirical method). To be consistent with S05 the abundances of our dwarf sample were also computed with the empirical method, and although the new L-Z relation has more scatter than the one using direct abundances, in this way our dwarf galaxies can be placed in a same graph together with the galaxies analyzed by S05. The slope and zero-point of the relation for our dwarfs, using indirect abundances, are different than those of the relation obtained with direct abundances, and, when compared to S05 giants, a possible break-point appears at $M_H \approx -20$. While this could suggest a different gas-consumption mechanism for dwarf and giant galaxies, a solid conclusion cannot be established at this stage. Indeed, the version of the empirical method employed by S05 is different from that classically used, and so a slight inconsistency between our abundances and those of S05 may still exist. The best way for giving the final word on this possible giant-dwarf dichotomy would be to obtain direct abundances for a good number of the KISS galaxies. And precisely, such a project has been started recently by some of us (see Saviane et al. 2007).

One of the motivations for the current study was to remedy the lack of homogeneous abundances and luminosities in the literature, but still it was interesting to make the experiment of assembling an L-Z relation based on literature data, and see whether our approach really turned out to be superior. We concluded that indeed mixing data from a variety of sources builds

an L-Z relation affected by large uncertainties, and very different from the one obtained with a controlled sample and controlled methods. Inferences based on literature data are thus to be taken as qualitative at best, and should be discarded, if possible.

Limiting ourselves to our sample of dIrrs, we attempted to explain the L-Z relation assuming that the chemical evolution of these objects is similar to that of a closed-box model with an effective yield which is 1/3 its value in the solar vicinity (Skillman et al. 2003b, Pilyugin et al. 2004). If this approximation holds true, and if we assume that the chemical evolution has started at the same time irrespective of mass, then the conclusion is that more massive galaxies have faster chemical evolutions (gas-consumption rates). Alternatively, more massive galaxies had more time to build up their metal content.

Due to a number of reasons (mainly adverse weather conditions) we could assemble a large database only for the Sculptor group of galaxies, while only two galaxies of the M81 group enter our L-Z relation. Although these two dwarfs seem to follow the same relation as that defined by the Sculptor group galaxies, more M81 dIrrs need to be measured, before one can understand whether the higher density in that group is influencing the chemical evolution of its members.

Indeed in general terms our L-Z relation is based on a small number of galaxies, therefore more objects need to be added to Fig. 6 in order to confirm our L-Z relation with a larger sample. For example looking at the number of dIrr presented in Lee et al. (2006), we might be able to add ~ 20 galaxies to our database. And 10m-class facilities will have to be used to reach this goal in a reasonable time. In the short term we plan to keep collecting data for the M81 group, and start a similar study for the Centaurus A group. A natural extension of the project would be to investigate clusters of galaxies, but this is a difficult task from the observational point of view, since the two nearest galaxy clusters are Virgo and Fornax, at 22 and 24 Mpc respectively (Ferguson & Sandage 1990; hereafter FS90). A more viable alternative would be to observe the Leo group of galaxies. At a distance of 18.2 Mpc (FS90), this group is the fourth nearest one, and has a relatively high velocity dispersion of 250 km sec $^{-1}$. Its properties (density, number of galaxies, dwarf-to-giant galaxy ratio, etc.) are intermediate between those of nearby groups and those of clusters of galaxies (see e.g. Figure 1 and following in Ferguson & Sandage 1991). It would then allow us to begin the exploration of a cluster-like environment, with NIR cameras at 10m-class telescopes.

Acknowledgements. This research has made use of the NASA/IPAC Extragalactic Database (NED) which is operated by the Jet Propulsion Laboratory, California Institute of Technology, under contract with the National Aeronautics and Space Administration. We thank John Salzer for providing the data of KISS galaxies in tabular form, and the referee for providing useful comments that improved the presentation of our work. Regina Riegerbauer, Nadia Millot, and Richard Whitaker helped with the data reductions at different stages of this project. This paper is dedicated to the memory of Maria Saviane.

References

- Alloin, D., Collin-Souffrin, S., Joly, M., & Vigroux, L. 1979, *A&A*, 78, 200
- Bica, E., Alloin, D., & Schmidt, A. 1990 *MNRAS*, 242, 241
- Bouchard, A., Jerjen, H., Da Costa, G. S., & Ott, J. 2005 *AJ*, 130, 2058
- Bruzual, G., & Charlot, S. 1983, *ApJ*, 405, 538
- Bruzual, G., & Charlot, S. 2003, *MNRAS*, 344, 1000
- Buzzoni, B., Delabre, B., Dekker, H., et al. 1984, *Msngr*, 38, 9
- Cairós, L.M., Caon, N., Papaderos, P., et al. 2003, *ApJ*, 593, 312
- Caldwell, N. Armandroff, T. E., Seitzer, P., & Da Costa, G. S. 1992, *AJ*, 103, 840
- Caldwell, N., Armandroff, T. E., Da Costa, G. S., & Seitzer, P. 1998, *AJ*, 115, 535
- Calura, F., & Matteucci, F. 2006, *MNRAS*, 369, 465

- Cardelli, J. A., Clayton, G. C., & Mathis, J. S. 1989, *ApJ*, 345, 245
- Chiosi, C., & Carraro, G. 2002, *MNRAS*, 335, 335
- Côté, S., Freeman, K. C., Carignan, C., & Quinn, P. J. 1997, *AJ*, 114, 1313 (C97)
- Dekel A., & Silk, J. 1986, 1986, *ApJ*, 303, 39
- Dufour, R. J., Garnett, D. R., & Shields, G. A. 1988, *ApJ*, 332, 752
- Edmunds, M. G. & Pagel, B. E. J. 1984, *MNRAS*, 211, 507 (EP)
- Ferguson, H. C., & Sandage, A. 1990, *AJ*, 100, 1
- Ferguson, H. C., & Sandage, A. 1991 *AJ*, 101, 765
- French, H. B. 1981, *ApJ*, 246, 434
- Froebrich, D. & Meusinger, H. 2000, *A&AS*, 145, 229 (FM00)
- Garnett, D. R. 1989, *ApJ*, 345, 282
- Garnett, D. R. 2002, *ApJ*, 581, 1019
- Gil de Paz, A., Madore, B. F., & Pevunova, O. 2003, *ApJS*, 147, 29
- Grebel, E. K. 2004, In: *Carnegie Observatories Astrophysics Series, Vol 4: Origin and Evolution of the Elements*, ed. A. McWilliam and M. Rauch (Cambridge: Cambridge Univ. Press) 2004, p. 237
- Hamuy, M., Walker, A. R., Suntzeff, N. B., Gigoux, P., Heathcote, S. R., & Phillips, M. M. 1992, *PASP*, 104, 533
- Hamuy, M., Suntzeff, N. B., Heathcote, S. R., Walker, A. R., Gigoux, P., & Phillips, M. M. 1994, *PASP*, 106, 566
- Hidalgo-Gómez, A. M. & Olofsson, K. 1998, *A&A*, 334, 45
- Hidalgo-Gómez, A. M., & Olofsson, K. 2002, *A&A*, 389, 836
- Hidalgo-Gómez, A. M., Sánchez-Salcedo, F. J., & Olofsson, K. 2003, *A&A*, 399, 63 (H03)
- Hirashita, H., Hunt, L. K., Ferrara, A., 2002, *MNRAS*, 330, L19
- Hummer, D. G., & Storey, P. J. 1987, *MNRAS*, 224, 801
- Hunter, D. A., & Hoffman, L. 1999, *AJ*, 117, 2789 (HH99)
- Hunter, D. A., & Elmegreen, B. G. 2004, *AJ*, 128, 2170
- Hunter, D. A. & Elmegreen, B. G. 2006, *ApJS*, 162, 49
- Hunt, L. K., Mannucci, F., Testi, L., et al. 1998, *AJ*, 115, 2594
- Izotov, Y. I., & Thuan, T. X. 1997, *ApJS*, 108, 1
- Izotov, Y. I., Thuan, T. X., & Lipovetsky, V. A. 1997, *ApJS*, 108, 1 (I97)
- Izotov, Y. I., & Thuan, T. X. 1998, *ApJ*, 500, 188
- Izotov, Y. I., & Thuan, T. X. 2004, *ApJ*, 602, 200
- James, P. A., Shane, N. S., Beckman, J. E., et al. 2004, *A&A*, 414, 23
- Jarrett, T., Chester, T., Cutri, R., et al. 2000, *AJ*, 119, 2498
- Jerjen, H., Freeman, K. C., & Binggeli, B. 1998, *AJ*, 116, 2873 (J98)
- Karachentseva, V. E., Karachentsev, I. D. & Borngen, F. 1985, *A&AS*, 60, 213 (KKB)
- Karachentseva, V. E. & Karachentsev, I. D. 1998, *A&AS*, 127, 409
- Karachentsev, I. D., Dolphin, A. E., Geisler, D., et al. 2002, *A&A*, 383, 125 (K02)
- Karachentsev, I. D., Karachentseva, V. E., Huchtmeier, W. K., & Makarov, D. I. 2004, *AJ*, 127, 2031
- Kennicutt, R. C., Jr., Bresolin, F., & Garnett, D. R. 2003, *ApJ*, 591, 801 (KBG)
- Kobulnicky, H. A., & Skillman E. D. 1996, *ApJ*, 471, 211
- Larson, R. B. 1974, *MNRAS*, 169, 229
- Lee, H., Skillman, E. D., Cannon, J. M., et al. 2006, *ApJ*, 647, 970
- Lee, J. C., Salzer, J. J., & Melbourne, J. 2004, *ApJ*, 616, 752
- Lynden-Bell, D. 1992, in *Elements and the Cosmos. Proceedings of the 31st. Herstmonceux Conference*, held in Cambridge, England July 16-20 1990, Edmunds M. G. & Terlevich R. (eds.), Cambridge University Press. P. 270
- Maeder, A. 1992, *A&A*, 264, 105
- Marcolini, A., D'Ercole, A., Brighenti, F., Recchi, S., 2006, *MNRAS*, 371, 643
- Martin, C. L. 1997, *ApJ*, 491, 561
- Martin, C. L., Kobulnicky, H. A., & Heckman, T. M. 2002, *ApJ*, 574, 663
- Mateo, M. 1998 *ARA&A*, 36, 435
- Mendes de Oliveira, C. L., Temporin, S., Cypriano, E. S., et al. 2006, *AJ*, 132, 570
- Miller, B. W. 1996, *AJ*, 112, 991 (M96)
- Moorwood, A., Cuby, J. G., & Lidman, C. 1998, *The Messenger* 91, 9
- Oke, J. B. 1990, *AJ*, 99, 1621
- Osterbrock, D. E. 1989, *Astrophysics of gaseous nebulae and active galactic nuclei*, University Science Books
- Persson, S. E., Murphy, D. C., Krzemiński, W., Roth, M., & Rieke, M. J. 1998, *AJ*, 116, 2475
- Pilyugin, L. S. 2000, *A&A*, 362, 325 (P00)
- Pilyugin, L. S., & Ferrini, F. 2000, *A&A*, 358, 72
- Pilyugin, L. S. 2001, *A&A*, 374, 412 (P01)
- Pilyugin, L. S., Vilchez, J. M., & Contini, T. 2004, *A&A*, 425, 849
- Richer, M. G. & McCall, M. L. 1995, *ApJ*, 445, 642
- Roy, J.-R., Belley, J., Dutil, Y., & Martin, P. 1996, *ApJ*, 460, 284 (R96)
- Salzer, J. J., Lee, J. C., Melbourne, J., et al. 2005, *ApJ*, 624, 661 (S05)
- Saviane, I., Rizzi, L., Held, E. V., Bresolin, F., & Momany, Y. 2002, *A&A*, 390, 59
- Saviane, I., Riegerbauer, R., Held, E. V., et al. 2004, *IAUS*, 217, 200
- Saviane, I., Held, E. V., Ivanov, V., et al. 2005. In: *Near-fields cosmology with dwarf elliptical galaxies*, *proc. IAU Coll. 198*, Jerjen, H., & Binggeli, B. (eds.) Cambridge University Press. p. 202
- Saviane, I., Bresolin, F., & Salzer, J. 2007, In "From Stars to Galaxies: Building the pieces to build up the Universe" (Venice, October 16-20, 2006). ASPC, 374, 99
- Schlegel, D. J., Finkbeiner, D. P., & Davis, M. 1998, *ApJ*, 500, 525
- Schmidt, M. 1959, *ApJ*, 129, 243
- Schmidt, A. A., Alloin, D., & Bica, E. 1995, *MNRAS*, 273, 945
- Searle, L., & Sargent, W. L. W. 1972, *ApJ*, 173, 25
- Shi, F., Kong, X., Li, C., & Cheng, F. Z. 2005, *A&A*, 437, 849
- Silich, S. A., Tenorio-Tagle, G., 1998, *MNRAS*, 299, 249
- Skillman, E. D., Kennicutt, R. C., & Hodge, P. W. 1989, *ApJ*, 347, 875
- Skillman, E. D., & Kennicutt, R. C. 1993, *ApJ*, 411, 655 (SK03)
- Skillman, Evan D., Côté, S., & Miller, B. W. 2003a, *AJ*, 125, 593 (S03a)
- Skillman, E. D., Côté, S., & Miller, B. W. 2003b, *AJ*, 125, 610 (S03b)
- Stasinska, G. 1978, *A&A*, 66, 257
- Storchi-Bergmann, T., Calzetti, D., & Kinney, A. L. 1994, *ApJ*, 429, 572
- Thuan, T. X. 1983, *ApJ*, 268, 667
- Thuan, T. X., & Izotov, Y. I. 2005, *ApJ*, 627, 739 (TI05)
- Thuan, T. X., & Izotov, Y. I. 2005, *ApJS*, 161, 240
- Tinsley, B. M., & Larson, R. B. 1979, *MNRAS*, 186, 503
- Tonry, J. L., Blakeslee, J. P., Ajhar, E. A., Dressler, A., 2000, *ApJ*, 530, 625
- Tosi, M., Greggio, L., Focardi, P., & Marconi, G. 1992, *IAU Symp.*, 149, 207
- Tremonti, C. A., Heckman, T. M., Kauffmann, G., et al. 2004, *ApJ*, 613, 898
- Vaduvescu, O., McCall, M. L., Richer, M. G., & Fingerhut, R. L. 2005, *AJ*, 130, 1593
- van Zee, L., Haynes, M. P., & Salzer, J. J. 1997, *AJ*, 114, 2479
- van Zee, L., Westpfahl, D., Haynes, M. P., Salzer, J. J., 1998, *AJ*, 115, 1000
- Vanzi, L., Hunt, L. K., Thuan, T. X., & Izotov, Y. I. 2000, *A&A* 363, 493
- Vigroux, L., Stasinska G., & Comte G. 1987, *A&A*, 172, 15

Appendix A: Reduction of EFOSC2 long-slit spectroscopy

A.1. Extraction of spectra

All nights were treated separately, and reductions were carried out using a customized version of the EFOSC2 quick-look tool (<http://www.ls.eso.org/>), which is based on the ESO-MIDAS data reduction system. The main reduction steps are summarized as follows.

All bias frames were inspected to ensure that their level was the same, and an average bias was then computed and subtracted from the rest of the frames. The master flatfield was computed by taking the median of five normalized frames and then subtracting the spectral signature of the quartz lamp. The latter was computed by first averaging the flux along the spatial direction, then fitting a polynomial of degree 6 along the dispersion, and finally expanding it back into a bidimensional frame. The wavelength calibration was computed based on the spectrum of the internal Helium-Argon lamp, taken with the 1" wide slit. Since the projection of the 5" wide slit on the CCD is in the same position, the calibration was used both for the spectra of the H II regions and the spectrophotometric standards. A transformation of the form $(x, y) \rightarrow (\lambda, s)$ was found, thus correcting also for the distortion of the spectra introduced by the optical system. The transformation was modeled with polynomials of degree 3 and 2 along the dispersion and the spatial direction, respectively. After applying the calibration, the spectra were linearly rebinned with a constant step of $\Delta\lambda = 4.23\text{\AA}$. The bidimensional sky frame was created by first sampling the sky spectrum in two windows flanking the target spectrum, and then fitting the spatial gradient with a polynomial of degree 1. After subtracting the sky frame, the extraction window of the emission-line spectra was decided by looking at the spatial profile of the H α line and making some experiments until the best S/N was found. On the other hand, the flux of the spectrophotometric standard stars was summed over almost the entire spatial profile, leaving out just the two sky windows. As it was recalled above, the response function for the flux calibration was computed using the star LTT 3218. To

do this, the instrumental spectrum was corrected for atmospheric extinction, divided by the exposure time, and then divided by the published spectrum, and the ratio was fitted with a polynomial of degree 12. The spectrophotometric standard was observed at several airmasses, and we checked that the extinction-corrected and normalized spectra are almost identical, thus confirming the extinction curve for La Silla provided by MIDAS. The response function was then computed as the median of the five functions found for the two nights. The pre-processed, wavelength-calibrated, sky-subtracted and extracted spectra were thus finally flux-calibrated using this response function.

A.2. Flux measurements

The fluxes were measured within the ALICE CONTEXT in MIDAS. A fourth-degree continuum was fitted to the line-free spectra, and then for each line the flux was summed within two wavelengths bracketing the line. The blends $H\gamma + [O III] \lambda 4363$, $H\alpha + [N II] \lambda 6583$ and the $[S II]$ doublet $\lambda \lambda 6716, 6731$ were deconvolved using Gaussian fits, and we ensured that the sum of the single line fluxes equaled that of their blend. The measured line ratios were corrected for the effects of reddening, measured by comparing the observed and the expected hydrogen line ratios. The theoretical H line ratios of Hummer & Storey (1987) were used, assuming an electron temperature $T_e \approx 10000$ K. We set $R = I_\lambda / I_{H\beta}$, $R_0 = I_{\lambda,0} / I_{H\beta,0}$ and $\varphi(\lambda) = [f(\lambda) - f(H\beta)]$ so that $C = [\log R_0 / R] / \varphi(\lambda)$. The reddening constant was then computed using the Cardelli et al. (1989) extinction law, where $f(\lambda) = A(\lambda) / A(V)$, and we assumed $R_V = 3.1$. We obtained the value of C both from the ratio $H\alpha / H\beta$ and from $H\beta / H\gamma$. These line ratios are affected by the unknown stellar absorption under the H emission lines: we then corrected the fluxes assuming a constant EW of the absorption lines, and adopted the EW that yielded the closest values for the two C . In some cases we were not able to resolve $H\alpha$ from the $[N II]$ lines; however, the flux of the latter lines is at most a few percent of that of $H\alpha$, so we assumed that this correction is negligible. Since the $H\alpha / H\beta$ ratio is the more accurate, the value from this ratio was adopted to correct the observed fluxes, which were finally normalized to $H\beta$ whose flux was set to 1.

Appendix B: Reduction of KAST long-slit spectroscopy

B.1. Extraction of spectra

In the following we will call blue, red, full, and high-resolution, the spectra taken with the blue arm and grism 830/3460, with the red arm and grating 300/4230 (plus dichroic D46), with the red arm and no dichroic, and with the red arm and grating 1200/5000, respectively.

The frame pre-processing, wavelength calibration, and flux calibration was done within ESO-MIDAS (and its “context” LONG), with a modified version of the quick-look tool described above. The procedure was similar to the EFOSC2 data reduction, except for the bias subtraction, which is done directly by the *Kast* acquisition system. All the frames were trimmed to remove the overscan regions, and then master flat-field (FF) and arc images were created. Three to five dome flat-field frames per spectrograph configuration were available, so a median frame was first created, and then the spectral signature of the lamp was removed by fitting a polynomial surface to the median FF, assuming that the polynomial does not vary along the spatial direction.

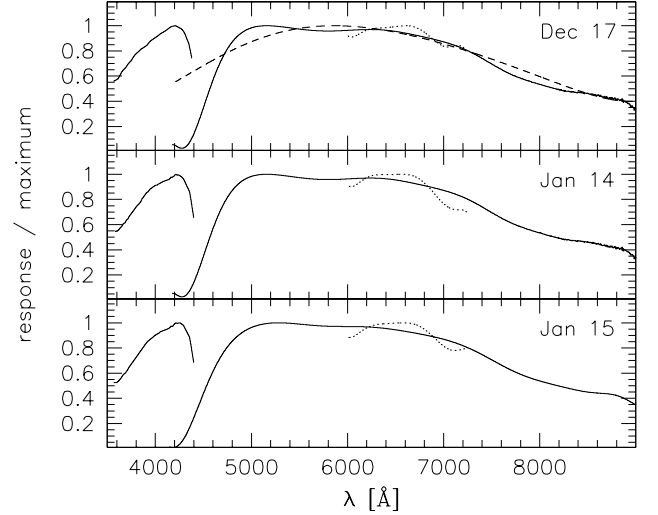


Figure B.1. Response functions for each date of the Lick run: the solid curves are the functions for the blue and red spectra, the dashed curve is the full spectrum function (no dichroic), and the dotted lines are the functions for the high resolution spectra. The functions have been normalized to the peak response.

Table B.1. Dispersions and wavelength range for each date and *Kast* configuration

<i>Kast</i> setup Arm/dichroic/grating grism	disp. [Å/px]	wavelength range	
Dec 17, 2001			
blue/D46/830_3460	1.1	3198.0	4532.2
red/D46/1200_5000	1.2	5856.5	7240.8
red/D46/300_4230	4.6	4216.2	9099.2
red/none/300_4230	4.6	3688.1	9097.7
Jan 14, 2002			
blue/D46/830_3460	1.1	3213.1	4552.3
red/D46/1200_5000	1.1	5874.4	7194.9
red/D46/300_4230	4.6	4170.7	9052.5
Jan 15 2002			
blue/D46/830_3460	1.1	3213.3	4552.7
red/D46/300_4230	4.6	4149.0	9032.9

Our main concern in the data reduction was to ensure that, in the overlap region, the fluxes of blue and red spectra are calibrated with the smallest systematic uncertainties. This was particularly difficult for the shortest wavelengths of the red spectra (blueward of ~ 5000 Å), where the response function drops steeply from 50% to zero in just ~ 300 Å (see below and Fig. B.1). This gradient is extremely sensitive to the FF correction in this spectral region, and it was found that a polynomial of degree 7 gave the best response function for the red spectra. For all other spectra a degree 6 polynomial gave the best results.

The arcs were used to remap the bidimensional spectra from the pixel-pixel space to the wavelength-pixel space, thereby also correcting the off-axis distortions of the optics, such that the spectrum could be extracted by just defining a window in the spatial direction. The two *Kast* lamps are filled with NeAr and HeHgCd, and since no cadmium or mercury line lists are avail-

able in the MIDAS system, a suitable line list was built from various sources. The computed dispersions and wavelength coverages for each *Kast* configuration are given in Table B.1. The dispersion is $\sim 1 \text{ \AA px}^{-1}$ for the blue and high resolution spectra, and 4.6 \AA px^{-1} for the red and full range spectra. The resolution, as measured on the arc lines, is $\sim 3 \text{ \AA FWHM}$ and $\sim 10 \text{ \AA FWHM}$ for the high and low resolution spectra.

In the next step, all the spectra were divided by the master FF and calibrated in wavelength, and then a preliminary extraction with a large window was done, in order to create sky images for each spectrum, that were used for the correction of the spectrograph flexures (see below). The sky frames were constructed by first creating the sky spectrum on the two sides of the central object, as an average within two windows. The flanking sky spectra were used to fit the sky gradient in the spatial direction, assumed to be linear and independent of wavelength, and the bidimensional artificial sky frames were made by simulating this gradient.

By comparing the position of sky lines in different spectra, it was soon realized that the spectrograph is subject to large flexures, with spectrum-to-spectrum differences of up to 10 px, i.e. more than 40 \AA for the red spectra. This fact has several implications, and at this point of the reduction it affects the definition of the response function, in particular at the shortest wavelengths of the red spectra. For this reason, the standard star spectra were registered to rest-frame wavelengths before creating the response function. Due to the short exposure times, the sky lines are almost absent from the standard star spectra, so the shift in wavelength was computed using the central wavelength of $H\alpha$ for the red spectra, and $H\gamma$ for the blue spectra. This approach works if the effect of radial velocities on the position of the stellar lines is negligible. This assumption was checked by comparing the relative position of $H\alpha$ and the telluric triplet at $\sim 6870 \text{ \AA}$. The average difference over all standard stars is $\Delta\lambda = 309.1 \pm 0.7 \text{ \AA}$, and since the scatter is much less than the spectral dispersion, we conclude that indeed the effect of radial velocities (both intrinsic and due to the solar motion) is negligible, and that the barycenter of the telluric triplet is at 6871.9 \AA .

The shift in wavelength was then subtracted from the starting wavelength of the bidimensional spectra, the standard star spectra were extracted again, and the response function was defined by comparison to the published spectrum. Again, the most difficult task is following the response function for the red spectra blueward of $\sim 5000 \text{ \AA}$. It was found that a polynomial fit is not adequate even using the highest degree implemented in MIDAS (30). We then used a spline of degree 1, which gave good results since the sample rate of the published fluxes is a few \AA . The master response function was decided by flux-calibrating all the standard stars with a given response function, and then by taking the one that gave the best average calibration for all standards and over a range of airmasses (see Fig. B.1). Due to the large wavelength coverage, the most critical case is that of the red spectra, where we expect a maximum difference of $\sim 5\%$ from the red to the blue part of the spectrum. For these spectra, the response function is able to correct the instrumental flux down to 4300 \AA .

Finally the galaxy spectra were extracted and flux-calibrated with a procedure resembling that adopted for the standard stars, but in this case the flexure correction was done with the very strong sodium sky line at 5892 \AA . In order to have a good subtraction of the sky lines, the sky windows were chosen close to the object spectrum, and the best windows were decided on an object-by-object basis with several experiments. Also the win-

dows for the object spectra needed a careful selection, in order to enhance the faint lines over the background, and to avoid as much as possible the places where the sky line subtraction was less than optimal.

B.2. Creation of merged spectra

Using the continuum in the overlap regions, the final spectra have been obtained by merging the blue, red (or full in the case of DDO 42), and high resolution spectra. This implies that a reliable merging could be produced only for those spectra where a meaningful continuum could be defined (i.e. those with the higher S/N), namely for the regions in DDO 42, DDO 53, and UGC 4483. First, the continua have been equalized in the overlap regions, and then the spectra have been rebinned to a common 1 \AA step, which is smaller than any of the other dispersions. The equalization of the continua has been done in the $\log(\lambda) - \log(\text{flux})$ plane: a straight line has been fitted to the continua, and then the difference d of the two fits at the midpoint of the overlap region has been taken. The normalization factor is then 10^d . In the merged spectrum $H\alpha$ belongs to the high-resolution spectrum, $H\beta$ belongs to the red (or full) spectrum, and $H\gamma$ belongs to the blue spectrum. These hydrogen lines were then used to perform some health checks on the merged spectra. Both $H\alpha$ and $H\beta$ are present in the red (or full) spectrum, so we first checked that the ratio of these two lines is the same in the merged spectrum as in the red (or full) spectrum. If that was not the case, corrections to the equalization factors were introduced. $H\gamma$ is present both in the blue and in the red (or full) spectrum, however in that spectral region the response function of the red (or full) spectrum reaches almost zero, so its flux is rather uncertain. Comparing the flux of this line in the two spectra is then not really meaningful, so we followed another approach. For the Sculptor group dwarfs, Table 4 shows that the average flux of $H\gamma$ is $0.46 \times H\beta$, with a dispersion of $0.04 \times H\beta$. Thus we made sure that no strong deviations from this value were obtained: if the $H\gamma$ flux was more than 3σ discrepant from the quoted value, we adjusted the equalization factor to bring the flux into agreement with the average value while maintaining a good overlap of the continua. This meant reducing the deviations to less than 2σ .

B.3. Flux measurements

Line fluxes were measured in the way described in Sect. A.2, regarding EFOSC2 measurements. The difference is that a different set of lines had to be deblended. In particular, $[\text{O II}] 3727$ was deblended from two nearby unknown lines at 3722 \AA and 3736 \AA , $[\text{O III}] 4363$ was deblended from $H\gamma 4340$, and finally the Gaussian deblending was employed to separate $[\text{O II}] 7320$ from $[\text{O II}] 7330$.

Appendix C: Reduction of near-IR imaging

The first step of the data reduction was to remove the sky background, and simultaneously, the dark current and bias. We subtracted from each object image the average of the preceding and the succeeding sky images. This strategy accounts for sky background variations with characteristic time comparable or a few times longer than the time spent at each pointing. For the first and the last object, we could only subtract the nearest sky image. Next, we carried out the flat field correction. A common median zero point was imposed to all available sky images, a median was obtained to produce a flat field, which was normalized to

unity. Then, all sky-subtracted object images were divided by the flat-field. The bad pixels were masked out and all object images were aligned and combined to produce a final image for each target. In addition, for the SOFI data, we carried out an illumination correction to account for the difference between the sky illumination and the illumination of the dome screen used for flat-fielding, as described on the instrument webpages. The entire data reduction was carried out with standard IRAF tasks.

The photometric calibration was carried out by observations of standard stars from Hunt et al. (1998) for the Northern objects, and from Persson et al. (1998) for the Southern ones. The INGRID data were photometrically calibrated with measurements of 129 standard stars in 13 fields from the night of Jan 16, 2003, and the SOFI data were calibrated with 13 standard stars observed during all nights. Some galaxies were observed twice at the NTT to verify the self consistency of the photometry and because the night of Oct. 15, 2002 was non-photometric, so all targets had to be re-observed during the next night with shorter integration times. Finally, the calibration of ESO 473-024 is based on a single standard, observed at the same airmass as the target. The transformation equations are:

$$H = h - (0.055 \pm 0.005) \times \sec(z) + (23.430 \pm 0.007) \quad (\text{C.1})$$

with r.m.s.=0.040 mag for INGRID,

$$H = h - (0.032 \pm 0.003) \times \sec(z) + (24.727 \pm 0.006) \quad (\text{C.2})$$

with r.m.s.=0.011 mag for the Oct 2002 SOFI run, and

$$H = h + (24.775 \pm 0.009) \quad (\text{C.3})$$

for the Aug 2003 SOFI run. Here the upper case indicates magnitudes in the standard system, and the lower case indicates the instrumental system.